

BACON: Band-limited Coordinate Networks for Multiscale Scene Representation

David B. Lindell

Dave Van Veen

Jeong Joon Park

Gordon Wetzstein

Stanford University

<http://computationalimaging.org/publications/bacon>

Abstract

Coordinate-based networks have emerged as a powerful tool for 3D representation and scene reconstruction. These networks are trained to map continuous input coordinates to the value of a signal at each point. Still, current architectures are black boxes: their spectral characteristics cannot be easily analyzed, and their behavior at unsupervised points is difficult to predict. Moreover, these networks are typically trained to represent a signal at a single scale, and so naive downsampling or upsampling results in artifacts. We introduce band-limited coordinate networks (BACON), a network architecture with an analytical Fourier spectrum. BACON has predictable behavior at unsupervised points, can be designed based on the spectral characteristics of the represented signal, and can represent signals at multiple scales without explicit supervision. We demonstrate BACON for multiscale neural representation of images, radiance fields, and 3D scenes using signed distance functions and show that it outperforms conventional single-scale coordinate networks in terms of interpretability and quality.

1. Introduction

Coordinate networks are an emerging class of neural networks that can be used to represent or optimize a broad format of signals including images, video, 3D models, audio waveforms, and more [38, 41, 48, 60, 62]. As opposed to storing discrete samples of signals in conventional array- or grid-based formats, neural representations approximate signals using a continuous function that is embedded in the learned weights of a fully-connected neural network. Given an input coordinate, these networks are trained to output the value of a signal at that point. Since even complex or high-dimensional signals can be flexibly optimized using a coordinate network, they have become popular for applications including view synthesis [41], image processing [56], 3D reconstruction [48], and neural rendering [66].

Yet, current coordinate networks are black box models that are designed to represent signals at a single scale. As a

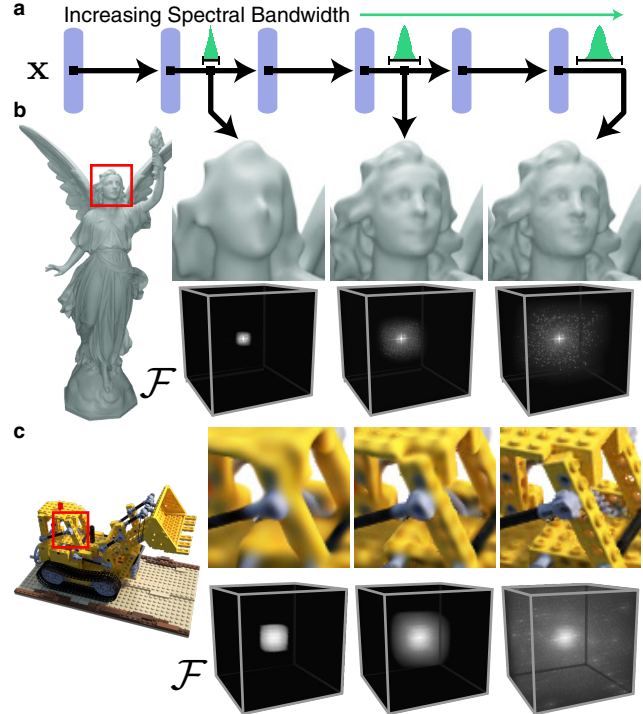


Figure 1. Overview of band-limited coordinate networks (BACON). (a) The proposed architecture produces intermediate outputs with an analytical spectral bandwidth that can be specified at initialization. When supervised on a high-resolution signal, the network learns a multi-resolution decomposition of the output, as shown for fitting 3D shapes via a signed distance function (b) and radiance fields (c). The network is characterized entirely by its Fourier spectrum (see insets) and so its behavior is predictable, even at unsupervised locations.

result, the behavior of the network at unsupervised coordinates is difficult to predict, with complex dependencies on hyperparameters such as hidden layer size, network depth, or input coordinate encoding. The black box nature of the architecture similarly inhibits multiscale signal representation, since we cannot readily filter or anti-alias these models, and the frequency spectrum of a coordinate network is

difficult to analyze. Thus naive downsampling or upsampling by querying the network on a coarser or finer grid of coordinates leads to aliasing or undesired high-frequency artifacts. Ultimately, these characteristics stem from the fact that coordinate networks are not amenable to Fourier analysis and are not designed to be scale aware.

Still, being able to represent and optimize signals at multiple resolutions is an important requirement for many applications. For example in image processing, many techniques rely on image pyramids [58] (e.g., optical flow estimation, compression, filtering, etc.). Representing 3D objects or scenes at multiple levels of detail is useful for speeding up rendering and reducing memory requirements (e.g., mipmapping).

In this work, we introduce band-limited coordinate networks (BACON). The key properties of this architecture are that (1) the maximum frequency at each layer can be manipulated analytically, and (2) the behavior of a trained network is entirely characterized by its Fourier spectrum. BACON is suited to multiscale signal representation because band-limited output layers can be designed with an inductive bias towards a particular resolution or scale.

In addition to introducing BACON, we demonstrate a variety of applications including multiscale representation of images, neural radiance fields, and 3D scenes. Our work takes important steps towards making coordinate-based networks scale aware, and provides a new representation with interpretable behavior. Specifically, we make the following contributions:

- We introduce band-limited coordinate-based networks for representing and optimizing signals.
- We develop methods for spectral analysis of the architecture, and propose a principled, band-limited initialization scheme.
- We demonstrate that our architecture outperforms conventional single-scale coordinate networks for multiscale image fitting, neural rendering, and 3D scene representation.

2. Related Work

Neural Scene Representation and Rendering. Emerging neural scene representations promise 3D-structure-aware, continuous, memory-efficient representations for parts [18, 19], objects [3, 6, 12, 20, 39, 48, 72], or scenes [13, 24, 51, 60, 62]. These can be supervised with 3D data, such as point clouds, and optimized as either signed distance functions [3, 20, 24, 28, 39, 48, 51, 59, 62, 64, 73] or occupancy networks [9, 38]. Using neural rendering [66], representation networks can also be trained using multiview 2D images [4, 17, 25, 31–33, 36, 41, 42, 45–47, 52, 56, 62, 63, 69, 71, 72, 77, 78]. Temporally aware extensions [44]

and multimodal variants with part-level semantic segmentation [30] have also been proposed. Recent 3D-aware GANs use related ideas but are training with 2D image collections [7, 43, 57].

Architectures for Scene Representation. Neural network architectures for scene representation networks can be roughly classified as feature-based, coordinate-based, or hybrid. Feature-based approaches represent the scene using differentiable feature primitives, such as points [14, 50, 53, 70, 75], surface patches [74], meshes [21, 55, 67, 79], multi-plane [16, 40, 80] or multi-sphere [2, 5] images, or using a voxel grid of features [34, 61]. A tradeoff with feature-based representations is that they can be quickly evaluated, but typically have a large memory footprint.

Coordinate-based representations (sometimes called implicit representations or coordinate networks), use a multilayer perceptron (MLP) to map from an input coordinate to a signal value, for example, the signed distance or occupancy of a 3D scene. These networks can represent complex, high-dimensional signals with a small memory footprint and represent signals continuously across the input domain. Ultimately, the maximum resolution of coordinate networks is tied to the capacity of the network architecture through dependencies on the number of trainable parameters and other architectural choices. There are varieties of coordinate networks that represent signals globally [38, 48, 60, 65] or locally [6, 8, 24, 54]. Hybrid architectures that combine feature-based and coordinate representations aim to combine the best of both worlds [22, 32, 35, 51].

The proposed method is also a coordinate network, but rather than using an MLP architecture, as with all coordinate networks discussed above, our method builds on recently proposed multiplicative filter networks (MFNs) [15]. We develop the theory of MFNs significantly, with new tools to describe and manipulate the Fourier spectra of these networks, and a new initialization scheme that mitigates vanishing activations in deep networks. These insights enable band-limited coordinate networks, which we demonstrate for multiscale signal representation.

Multiscale Representations. Several existing works have explored multiscale architectures in the context of scene representation networks. For example, proposed methods use an octree [64, 76] to accelerate neural rendering of radiance fields or signed distance functions, or a hierarchy of features [10] to improve 3D shape completion. Multiscale representations can be optimized directly using specialized architectures [35, 73] or progressive training strategies [23, 35]. The closest work to ours in this category is Mip-NeRF [4], which is a coordinate-based network with a scale-dependent positional encoding. After training the network with supervision at multiple scales, the resolution of the network output can be controlled by adjusting the positional encoding. Our work differs in that the bandwidth of

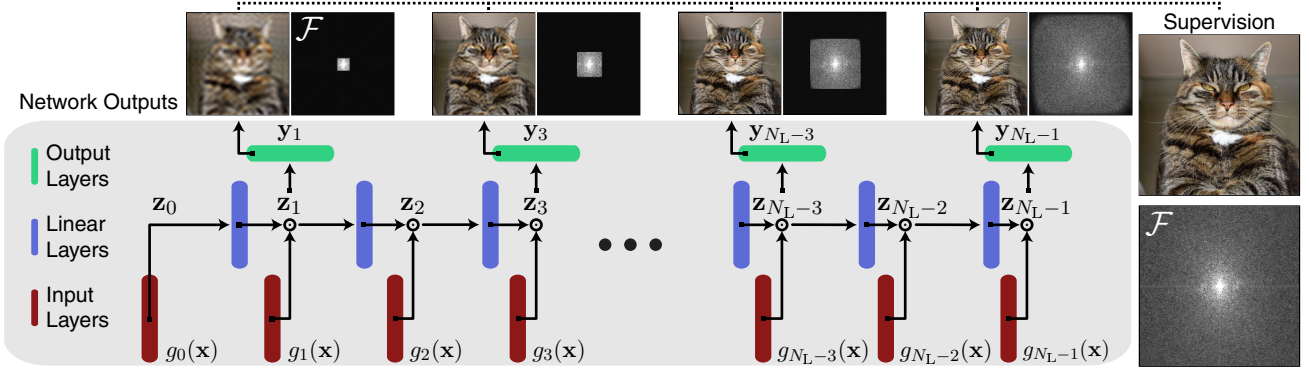


Figure 2. Overview of BACON architecture. We initialize the frequencies of the sine layers of a multiplicative filter network [15] within a limited bandwidth $[-B_i, B_i]$ (bottom row). Then, the bandwidth of each output layers is the sum of the input bandwidths up to that point (top row), allowing the network bandwidth to be explicitly specified. At training time the network can be supervised with a signal at any resolution, and the network learns to fit the signal in a band-limited fashion. Image from DIV2K dataset [1].

the network outputs are constrained by design rather than through training. Thus, our approach learns a band-limited multiscale decomposition of a signal, even without explicit training at multiple scales.

3. Method

This section, provides an overview of MFNs and the BACON multiscale architecture, describes the Fourier spectra of these networks, and proposes an initialization scheme for deep networks.

3.1. Band-limited Coordinate Networks

Our approach builds on a recently introduced coordinate-based architecture called Multiplicative Filter Networks (MFNs) [15], which differ from conventional MLPs in that they employ a Hadamard product between linear layers and sine activation functions. While BACON uses an MFN backbone, we significantly extend the theoretical understanding and practicality of these networks by (1) proposing architectural changes to achieve multiscale, band-limited outputs, (2) deriving formulas to quantify the expected frequencies in the representation, and (3) deriving a principled initialization scheme that prevents vanishing activations in deep networks.

In a forward pass through the network, an input coordinate $\mathbf{x} \in \mathbb{R}^{d_{\text{in}}}$ is first passed through several layers of the form $g_i : \mathbb{R}^{d_{\text{in}}} \mapsto \mathbb{R}^{d_h}$, with $g_i(\mathbf{x}) = \sin(\omega_i \mathbf{x} + \phi_i)$, $i = 0, \dots, N_L - 1$, and N_L the number of layers in the network. We refer to the intermediate activations as $\mathbf{z}_i \in \mathbb{R}^{d_h}$, and we allow intermediate outputs of the network $\mathbf{y}_i \in \mathbb{R}^{d_{\text{out}}}$ at the i th layer, defined as follows (see also Fig. 2).

$$\begin{aligned} \mathbf{z}_0 &= g_0(\mathbf{x}) \\ \mathbf{z}_i &= g_i(\mathbf{x}) \circ (\mathbf{W}_i \mathbf{z}_{i-1} + \mathbf{b}_i), \quad 0 \leq i < N_L \\ \mathbf{y}_i &= \mathbf{W}_i^{\text{out}} \mathbf{z}_i + \mathbf{b}_i^{\text{out}}, \end{aligned} \quad (1)$$

where \circ indicates the Hadamard product. The parameters of the network are $\theta = \{\omega_i \in \mathbb{R}^{d_h \times d_{\text{in}}}, \mathbf{b}_i, \phi_i \in \mathbb{R}^{d_h}, \mathbf{W}_i \in \mathbb{R}^{d_h \times d_h}, \mathbf{W}_i^{\text{out}} \in \mathbb{R}^{d_h \times d_{\text{out}}}, \mathbf{b}_i^{\text{out}} \in \mathbb{R}^{d_{\text{out}}}\}$.

A useful property of this formulation is that the network output can be expressed equivalently as a sum of sines with varying amplitude, frequency, and phase [15].

$$\mathbf{y}_i = \sum_{j=0}^{N_{\text{sine}}^{(i)}-1} \bar{\alpha}_j \sin(\bar{\omega}_j \mathbf{x} + \bar{\phi}_j), \quad (2)$$

where $\bar{\alpha}_i$, $\bar{\omega}_i$, and $\bar{\phi}_i$ depend on the parameters of the MFN, and the number of terms in the sum for an N_L layer network is given as (see supplemental for derivation)

$$N_{\text{sine}}^{(N_L)} = \sum_{i=0}^{N_L-1} 2^i d_h^{i+1}. \quad (3)$$

This property stems from the repeated Hadamard product of sines and the trigonometric identity that

$$\sin(a) \sin(b) = \frac{1}{2} (\sin(a + b - \pi/2) + \sin(a - b + \pi/2)). \quad (4)$$

By applying this identity through the layers of the network, the output can be reduced to a single sum of sines.

3.2. Frequency Spectrum

We exploit the property that MFNs can be expressed as a sum of sines to create band-limited networks. This is achieved by designing the architecture so that the frequency of all represented sines never exceeds a desired threshold.

To this end, we freeze (i.e., do not optimize) the frequencies, or entries of ω_i , and set them to a bandwidth in $[-B_i, B_i]$ using random uniform initialization. Then, since products of sines result in summed frequencies (Eq. 4), the total bandwidth of an output at layer i of the network is less

than or equal to $\sum_{j=0}^i B_j$ and the maximum bandwidth is $B = \sum_{i=0}^{N_L-1} B_i$ (see Fig. 2).

When representing signals across a finite input domain, e.g., with input coordinates $\mathbf{x} \in [-0.5, 0.5]^{d_{\text{in}}}$, it is not necessary to represent all frequencies continuously. Instead, we can assume that the represented signal is periodic, so we are only required to represent discrete frequency values whose spacing is $1/T$, where T is the periodicity or extent of the signal in the primal domain. Moreover, using discrete frequencies allows complete characterization of the network spectrum by applying a fast Fourier transform to a uniformly sampled network output (shown in Fig. 2 for image fitting).

We also analyze the distribution of sine frequencies in the network. Briefly, sines in the network can be associated with one of the N_L terms in the summation of Eq. 3. Then, considering the probability of sines originating from each term results in a compound random variable that gives the overall distribution of frequencies. We provide an extended derivation in the supplemental, showing that the distribution is approximately zero-mean Gaussian with variance

$$\text{Var}(\omega_i) \cdot \sum_{m=0}^{N_L-1} m \cdot \frac{2^{N_L-1-m} d_h^{N_L-m}}{\sum_{i=0}^{N_L-1} 2^i d_h^{i+1}}. \quad (5)$$

In practice, this Gaussian distribution of frequencies results in a greater parameterization of low frequencies in the network; this may be a useful inductive bias since low-frequency Fourier coefficients typically have a much higher amplitude than high-frequency coefficients in natural signals [68].

To facilitate representing signals at multiple resolutions, we introduce linear layers at intermediate stages throughout the network to extract band-limited outputs (see Fig. 2). By supervising the outputs of these layers, we can train BACON to fit a signal at multiple scales simultaneously. Interestingly, because the outputs are band-limited, BACON can be trained in a semi-supervised fashion where the bandwidth of the supervisory signal need not match the desired bandwidth of the output of the network, demonstrated in Fig. 2 for image fitting.

3.3. Initialization Scheme

Finally, we derive a principled initialization scheme that ensures the distribution of activation functions at the output of each layer is distributed uniformly at the beginning of training. We compare our initialization scheme to the initialization proposed by Fathony et al. [15] in Fig. 3. Our proposed scheme resolves a problem with vanishingly small activations for deep networks and results in standard normal distributed activations after each linear layer.

In the supplemental, we provide an extended derivation, which we summarize as follows. Assume the input to the

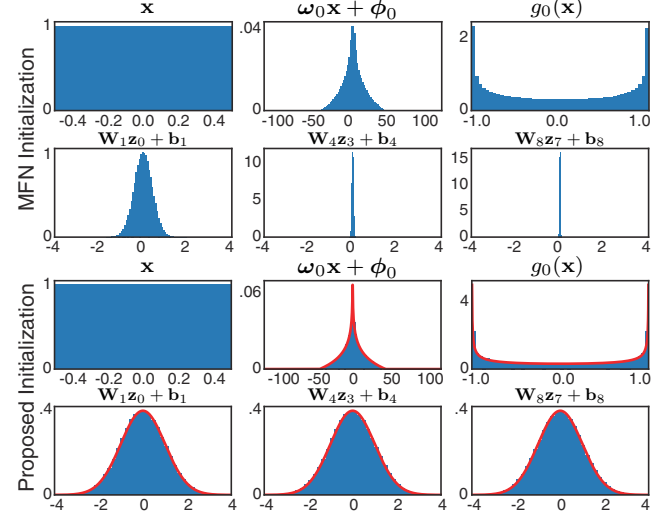


Figure 3. Comparison of distribution of activations at initialization. The initialization scheme proposed for MFNs [15] results in vanishingly small activations for deep networks (shown for layers 0, 1, 4, and 8). The proposed initialization scheme maintains a standard normal distribution after each linear layer (all distributions shown for a network with $d_h = 1024$), and activations at intermediate outputs closely match our analytical derivations (red lines, see supplemental for details).

network is uniformly distributed $\mathbf{x} \sim \mathcal{U}(-0.5, 0.5)$, with $\omega_i \sim \mathcal{U}(-B_i, B_i)$ and $\phi_i \sim \mathcal{U}(-\pi, \pi)$, where we describe the distribution of each element of the matrix or vector. Then, $\omega_i \mathbf{x} + \phi_i$ is distributed as

$$\begin{cases} 1/B_i \log(B_i / \min(|2x|, B_i)), & -B/2 \leq x \leq B/2 \\ 0 & \text{else} \end{cases}$$

and $g_i(\mathbf{x}) = \sin(\omega_i \mathbf{x} + \phi_i)$ is approximately arcsine distributed with variance 0.5 (see supplemental, red plots in Fig. 3). Now, let $\mathbf{W}_i \sim \mathcal{U}[-\sqrt{6/d_h}, \sqrt{6/d_h}]$. Then we have that $\mathbf{W}_1 g_0(\mathbf{x}) + \mathbf{b}_1$ converges to the standard normal distribution with increasing d_h (see supplemental). Finally, the Hadamard product $g_1(\mathbf{x}) \circ (\mathbf{W}_1 \mathbf{z}_0 + \mathbf{b}_1)$ is the product of arcsine distributed and standard normal random variables which again has a variance of 0.5. Applying the next linear layer results in another standard normal distribution, which is also the case after all subsequent linear layers (see red plots of Fig. 3).

4. Experiments

We demonstrate BACON on three separate tasks: image fitting, multiview reconstruction using neural radiance fields, and 3D shape fitting using signed distance functions.

4.1. Image Fitting

We use an image fitting task to evaluate the performance of BACON and to demonstrate its band-limited behavior.



Figure 4. Image fitting results. We train networks using Fourier Features [65], SIREN [60], and integrated positional encoding (PE) [4] to fit an image at 256×256 ($1 \times$) resolution. We show network outputs at $1/4$ and $4 \times$ resolution. Fourier Features and SIREN fit to a single scale and show aliasing when subsampled. Integrated PE is explicitly supervised at $1/4$ and $1 \times$ resolution and learns reasonable anti-aliasing; however, all methods except BACON show high-frequency artifacts at $4 \times$ resolution (insets). BACON is supervised at a single scale and learns band-limited outputs that closely match a low-pass filtered reference image (see left column and Fourier spectra insets).

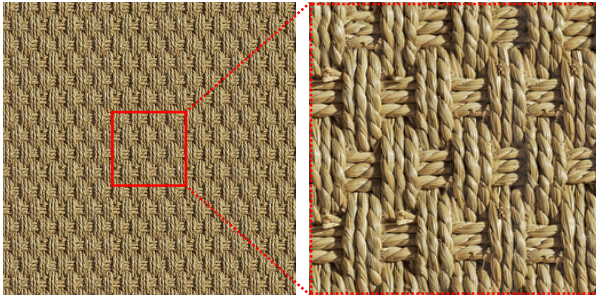


Figure 5. BACON periodic extrapolation behavior¹.

BACON is compared to three other baselines: a network with Gaussian Fourier Features positional encoding [65], SIREN [60], and the integrated positional encoding of Mip-NeRF [4], which is scale-dependent.

We initialize all networks with 4 hidden layers, 256 hidden features, and we train on the 256×256 resolution image for 5000 iterations using PyTorch [49] and Adam [29]. The batch size is set to be equal to the number of image pixels. For Fourier Features and integrated positional encoding, we use encoding scales of 6 and 10, respectively, which results in good reconstruction quality while reducing artifacts from overfitting. For SIREN, we initialize the frequency parameter to $\omega_0 = 30$.

Fourier Features and SIREN are trained to minimize the loss $\mathcal{L}_{\text{img}} = \|\mathbf{y} - \mathbf{y}_{\text{GT}}\|_2^2$, where \mathbf{y} is the network output and \mathbf{y}_{GT} are the image pixel values. For BACON, we sum this loss over all network outputs, with explicit supervision at all scales on the full-resolution image. The integrated positional encoding network is supervised explicitly on anti-aliased image pixels at $1/4$, $1/2$, and full resolution, following Barron et al. [4]. Finally, we initialize BACON to have a maximum bandwidth B of 0.5 cycles/pixel, which is the Nyquist limit for the image. The frequencies ω_i of BACON

are initialized so that the outputs \mathbf{y}_1 , \mathbf{y}_2 , and \mathbf{y}_4 are constrained to quarter, half, or full bandwidth. That is, we set $B_0 = B_1 = B/8$, and $B_2 = B_3 = B_4 = B/4$ such that $\sum_i B_i = B$.

Results of image fitting on a test scene from the Kodak dataset [11] are shown in Fig. 4. Since Fourier Features and SIREN only represent the signal at the trained resolution, sampling the network at $1/4$ resolution results in aliasing. We show the interpolation performance of these networks by evaluating a $4 \times$ upsampled grid of 1024×1024 pixels. The upsampled reference image shows image interpolation given by zero padding in the Fourier domain. All methods except BACON have non-zero high-frequency spectra and exhibit artifacts in the reconstruction. We show additional image fitting experiments in the supplemental.

Periodic Extrapolation. Since BACON uses discrete frequencies at each sine layer $g_i(\mathbf{x})$, the representation is periodic. We demonstrate this by fitting a seamless texture using coordinates $\mathbf{x} \in [-0.5, 0.5]$ (red square of Fig. 5) and querying the network output for $\mathbf{x} \in [-2, 2]$.

4.2. Neural Radiance Fields

Neural radiance fields (NeRF) [41] have become a popular method for multiview 3D reconstruction and neural rendering. The method operates on a dataset of multiview images with known camera positions, where each image pixel is associated with a ray $\mathbf{r}(t) = \mathbf{o} + t\mathbf{d}$ that extends from the camera center of projection \mathbf{o} in the direction \mathbf{d} passing through the pixel. A pixel color $\mathbf{C}(\mathbf{r})$ is predicted using the volume rendering equation to integrate predicted intermediate values of color \mathbf{c} and opacity σ along the ray [4]. In practice, a neural network is queried to evaluate samples of \mathbf{c} and σ along each ray $\mathbf{r}(t)$, and the volume rendering integral is evaluated using quadrature as [37, 40]

¹Image: <https://www.sketchuptextureclub.com/>

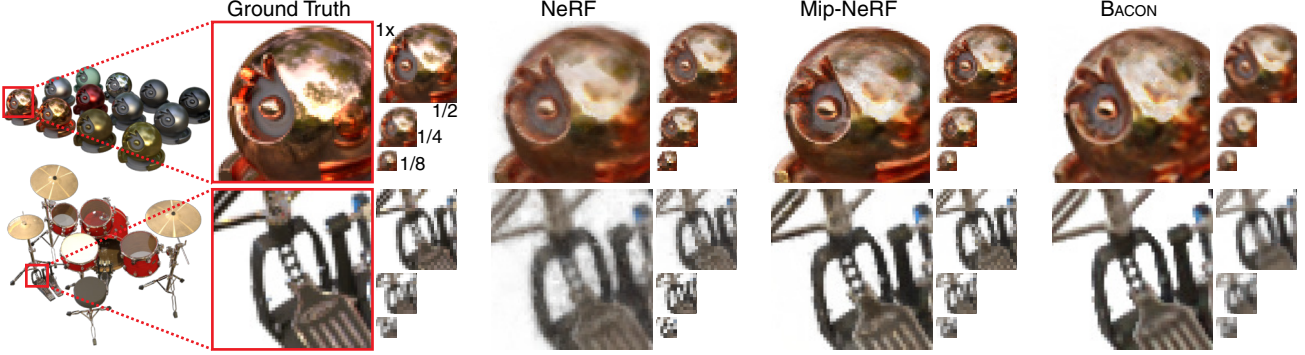


Figure 6. Neural rendering results. We compare NeRF [41], Mip-NeRF [4], and BACON supervised on a multiscale synthetic dataset [4]. BACON captures higher frequency details better than NeRF while requiring fewer parameters to render at 1/2, 1/4, and 1/8 resolution.

	PSNR ↑					# Params.			
	1x	1/2	1/4	1/8	Avg.	1x	1/2	1/4	1/8
NeRF	26.734	28.941	29.297	26.464	27.859	511K			
Mip-NeRF	29.874	31.307	32.093	32.832	31.526	511K			
BACON	27.430	28.066	28.520	28.475	28.123	531K	398K	266K	133K

Table 1. Performance of NeRF, Mip-NeRF, and BACON averaged across the multiscale Blender dataset. BACON achieves better average performance than NeRF while requiring fewer parameters to render the lower resolution images.

$$\mathbf{C}(\mathbf{r}, \mathbf{t}) = \sum_j T_j (1 - \exp(-\sigma_j(t_{j+1} - t_j))) \mathbf{c}_j, \quad (6)$$

with $T_j = \exp\left(-\sum_{i' < i} \sigma_{i'}(t_{i'+1} - t_{i'})\right)$,

where T_j represents the transmittance or visibility of a point on the ray, and the values $w_j = T_j(1 - \exp(-\sigma_j(t_{i+1} - t_j)))$ can be interpreted as alpha compositing weights applied to the predicted colors \mathbf{c}_j . After training, novel views can be rendered by simply evaluating the corresponding rays.

We evaluate BACON for this task and compare to NeRF and Mip-NeRF baselines trained on a multiscale Blender dataset [4] with images at full (512×512), 1/2, 1/4, and 1/8 resolution. For the baselines, we use the implementations of Barron et al.² [4]. All networks are trained according to the procedure of Mip-NeRF; we use the Adam optimizer with a batch size of 4096 rays and 1e6 training iterations. The learning rate is annealed logarithmically from 1e-3 to 5e-6 for BACON and 5e-4 to 5e-6 for the baselines. All networks are composed of 8 hidden layers with 256 hidden features.

For BACON, we adapt the training procedure and architecture as follows. Rays within the multiscale Blender dataset fall within an 8 by 8 unit volume ($\mathbf{r}(t) \in [-4, 4]^3$), and we find that setting the maximum bandwidth B to 64 cycles per unit interval allows fitting high frequency image details. To simplify the training procedure and improve the interpretability of the learned volume, we evaluate all methods without the viewing direction input originally used for NeRF. Thus the input to all networks is a

3D coordinate corresponding to the position along the ray $\mathbf{r}(t)$. BACON produces four outputs, one for each scale of the dataset: $\mathbf{y}_i, i \in [2, 4, 6, 8]$. The B_i constrain each output to 1/8, 1/4, 1/2, and full resolution, with $\sum_{i=0}^2 B_i = B/8$, $\sum_{i=0}^4 B_i = B/4$, and so on. We also adapt the hierarchical sampling procedure of NeRF [41], wherein the alpha compositing weights w_j from an initial forward pass are used to resample the ray in regions of non-zero opacity. To improve efficiency, we use the lowest-resolution output of the network for this initial forward pass and apply the following loss function on pixels rendered using the resampled rays with 256 samples.

$$\mathcal{L}_{\text{BACON}} = \sum_{i,j,k} \|(\mathbf{C}_k(\mathbf{r}_i, \mathbf{t}_j) - \mathbf{C}_{\text{GT},k}(\mathbf{r}_i)\|_2^2, \quad (7)$$

where i , j , and k index rays, ray positions, and dataset scales, respectively. Note that we explicitly supervise each output of BACON on the multiscale ground truth images to facilitate quantitative evaluation. Finally, we adopt the regularization strategy of Hedman et al. [22] to penalize non-zero off-surface opacity values (see supplemental).

Qualitative and quantitative evaluations of BACON for neural rendering, are shown in Fig. 6 and Table 1. BACON generally achieves better performance than NeRF trained on the multiscale dataset with the most dramatic improvement at 1/8 and 1x resolution. We report PSNR at each scale, averaged over all scenes in the multiscale Blender dataset in Table 1. In Fig. 6, we observe that BACON recovers higher frequency details compared to NeRF on the *Materials* and *Drums* scenes. Mip-NeRF incorporates an additional mechanism which changes the positional encoding along each ray to account for the expansion of the viewing frustum, and achieves the best performance. Still, we find that BACON produces high-quality novel view synthesis while using only a fraction of the parameters at low resolution.

Additionally, we can use BACON to learn semi-supervised multiscale decompositions of the neural radiance fields. In this case, we train each output scale at the full resolution, and BACON automatically learns band-limited representations at the intermediate output layers. We show

²<https://github.com/google/mipnerf>

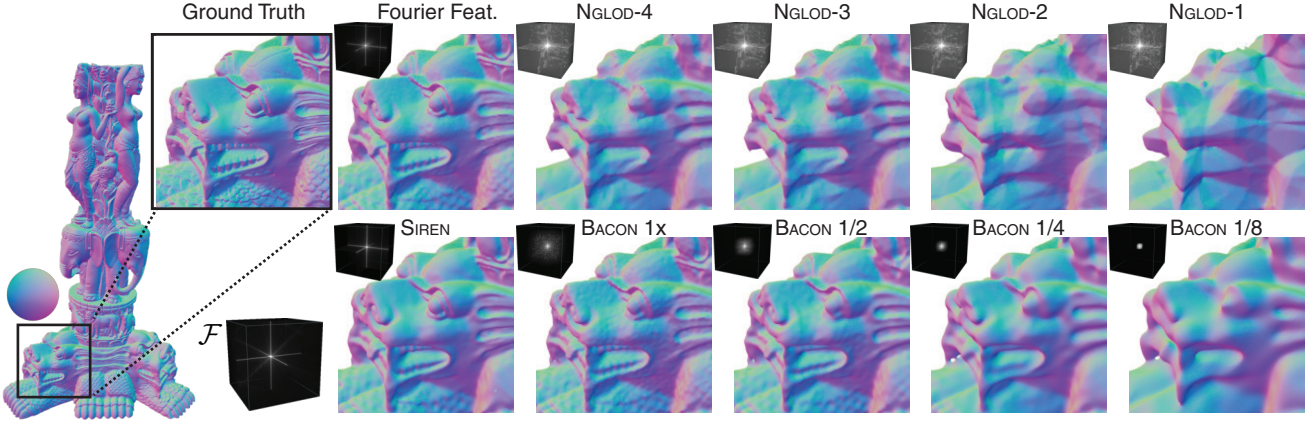


Figure 7. Shape fitting results. Results on the Thai Statue from the Stanford 3D Scanning Repository are shown for levels-of-detail 1–4 of Neural Geometric Level of Detail (NGLOD) [64], Fourier Features [65], SIREN [60], and BACON. All methods perform similarly at their highest detail output (see Table 2), but BACON learns a smooth multiscale decomposition of the shape. Insets show the spectra of the extracted signed-distance functions, revealing the band-limited output of BACON. Additional results included in the supplemental.

	FF	SIREN	NGLOD-4	NGLOD-5	BACON 1x
# Params.	527K	528K	1.35M	10.1M	531K
Chamfer↓	2.166e-6	2.780e-6	8.358e-6	2.422e-6	<u>2.198e-6</u>
IOU ↑	9.841e-1	9.751e-1	9.479e-1	9.811e-1	<u>9.833e-1</u>

Table 2. Shape fitting performance of Fourier Features [65], SIREN [60], Neural Geometric Level of Detail (NGLOD) [64], and BACON averaged across 5 test scenes (detailed in main text). All methods achieve roughly comparable performance, including BACON despite simultaneously representing multiple scales. Multiple levels of detail are shown for NGLOD, which require more parameters to populate the explicit feature grids.

an example of this for the *Lego* scene in Fig. 1. Additional results for BACON in the explicitly supervised and semi-supervised cases are shown in the supplemental.

4.3. 3D Shape Representation

Neural representation networks have shown promise for representing and manipulating 3D shapes. BACON is well-suited for this task, and we evaluate its performance on a range of shapes from the Stanford 3D scanning repository³.

We compare BACON to Fourier Features [65], SIREN [60], and Neural Geometric Level of Detail (NGLOD) [64], a representation which optimizes explicit features stored on a sparse voxel octree. All networks are trained to directly fit a signed distance function (SDF) estimated from a ground truth mesh.

For BACON, Fourier Features, and SIREN, we use networks with 8 hidden layers and 256 hidden features. For Fourier Features (Gaussian encoding), we set the encoding scale to 8 and for SIREN, we set $\omega_0 = 30$. We train on locations sampled from the zero level set and add Laplacian noise; this results in an exponential decay in the number of samples off the zero level, as proposed by Davies et al. [12].

We find that the width of the Laplacian distribution has a large impact on performance. Setting the variance σ_L^2 too small results in poor off-surface fitting, but setting the variance too high reduces the number of samples on the zero level set, degrading the appearance of the surface. Thus, we introduce a coarse and fine sampling procedure wherein we produce “fine” samples using a small variance of $\sigma_L^2 = 2e-6$ and “coarse” samples with $\sigma_L^2 = 2e-2$. Samples are drawn in the domain $[-0.5, 0.5]^3$, and we initialize the frequencies of BACON similar to the NeRF experiments (additional details in supplemental). We train using a loss function

$$\mathcal{L}_{\text{SDF}} = \lambda_{\text{SDF}} \|\mathbf{y}^c - \mathbf{y}_{\text{GT}}^c\|_2^2 + \|\mathbf{y}^f - \mathbf{y}_{\text{GT}}^f\|_2^2, \quad (8)$$

where \mathbf{y} is the network output, \mathbf{y}_{GT} represents the ground truth SDF values, the f and c superscripts indicate fine and coarse samples, and λ_{SDF} is a weight that we set to 0.01 for all experiments. For BACON we sum the loss at all outputs.

We train Fourier Features, SIREN, and BACON on each dataset for 200,000 iterations with a batch size of 5,000 coarse and 5,000 fine SDF samples. Models are optimized using Adam [29], and we logarithmically anneal the learning rate of each method from 1e-2 (BACON), 1e-3 (Fourier Features), and 1e-4 (SIREN) to a final value of 1e-4 during the course of training. For NGLOD, we use the default training settings in the authors’ code⁴, which samples 500,000 points at each training epoch, uses a batch size of 512, and trains for 250 epochs. We train NGLOD models with a maximum of 4 or 5 levels of detail. Additional levels of detail add successive layers in their octree representation, resulting in improved performance, but also an increased number of parameters.

We fit each method to four scenes from the Stanford 3D Scanning Repository (*Armadillo*, *Dragon*, *Lucy*, and *Thai Statue*), as well as a simple sphere baseline (all ob-

³<http://graphics.stanford.edu/data/3Dscanrep/>

⁴<https://github.com/nv-tlabs/nglod>

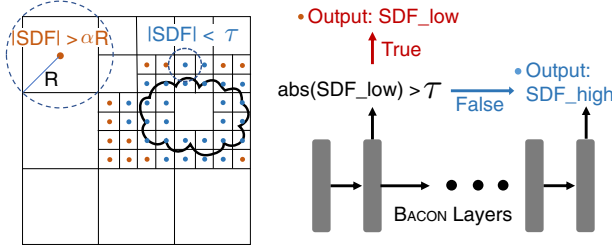


Figure 8. Adaptive-frequency multiscale SDF evaluation for fast mesh extraction. We propose a multi-scale evaluation which subdivides non-empty cells, i.e., when the SDF is smaller than the cell radius. We further accelerate the evaluation by using fewer layers (red) for regions that do not require high-frequency details. We evaluate the full network (blue) only when query locations are sufficiently close ($|SDF| < \tau$) to the surface.

Dense Grid (512 ³)	Adaptive-Frequency	Adaptive + Multiscale (Proposed)
Time (s)	17.91	5.50

Table 3. SDF evaluation time. The proposed Adaptive + Multiscale method achieves a roughly 80 \times speedup over naive evaluation of the SDF on a dense grid (averaged over 5 test scenes).

jects are shown in the supplemental). The models are extracted at 512³ resolution using marching cubes and evaluated using Chamfer distance and intersection over union (IOU), and we report these numbers averaged over the 5 scenes in Table 2. The highest resolution outputs of all methods achieve generally comparable performance, though note that NGLOD-5 requires over an order of magnitude more parameters than the other representations, and BACON achieves this despite representing all scales simultaneously.

We see similar qualitative trends in Fig. 7, with Fourier Features, SIREN, NGLOD-4, and BACON all producing detailed reconstructions of the *Thai Statue* scene. BACON produces a smooth reconstruction at multiple scales because of its band-limited output layers. This can be compared to the low-resolution outputs of NGLOD, which show fewer finer details, but also have coarse, angular artifacts from the ReLU non-linearity used in the network. This follows from the NGLOD frequency spectrum (see Fig. 7), which is non-zero for high frequencies, including at the coarsest scale.

Accelerated Marching Cubes. We observe that the band-limited, multi-output nature of our network allows efficient allocation of resources when evaluating SDFs on a dense grid for mesh extraction. The key idea is to use the lower-layer output of BACON when a cell is far away from the surface (Fig. 8). That is, we early-stop the computation within the network when $|SDF| < \tau$, where we set τ to 0.7 \times the finest voxel size. This adaptive computation significantly reduces the mesh extraction time (Table 3).

Moreover, we propose a multiscale approach for further acceleration. As SDF values indicate the distance to the closest surface, we can consider a cell to be empty

when $|SDF| > \alpha R$, for circumsphere radius R and some $\alpha > 1$ that improves robustness to imperfect SDFs (we use $\alpha = 2$). Starting from the coarsest resolution grid, we subdivide a cell only when $|SDF| < \alpha R$, efficiently pruning empty spaces, until the finest level. Multiscale extraction approaches have been proposed for extracting occupancy fields from coordinate networks [38], but using an SDF facilitates pruning since each sample reveals a region of empty space.

We combine the two strategies by applying the adaptive-frequency evaluation on each level of the multiscale grids, leading to roughly 80 \times faster SDF evaluation than the naive approach as shown in Table 3 (see supplemental results, all timings evaluated on an NVIDIA RTX A6000 GPU).

5. Conclusion

In this work we take important steps towards making coordinate networks interpretable and scale aware. Our approach enables analyzing and controlling the spectral bandwidth of the network at intermediate layers, allowing multiscale signal representation, even without explicit supervision. Since we can characterize the behavior of the network using Fourier analysis, its outputs are predictable, even at unsupervised locations. Moreover, BACON’s unique intermediate outputs can address the characteristic slow inference time of the coordinate-networks, via adaptive frequency evaluation. We show that BACON outperforms other single-scale coordinate networks for multiscale image fitting, neural rendering, and 3D scene representation.

Limitations. We also highlight a few limitations of BACON and promising future directions. In this work, we demonstrated BACON for representing two- and three-dimensional signals. Fitting signals in higher dimensions may require more parameters to achieve dense spectral coverage due to the curse of dimensionality. Still, it may be possible to optimize the initialization of frequencies in a way that maximizes spectral coverage and mitigates this challenge. Also, our current work is limited to single scene overfitting. However, many generative models work by increasing the frequency of the output using successive upsampling layers [27], which is similar in spirit to our method. Recent work on band-limited models for image synthesis has shown great promise [26], so applying BACON for generative modeling is an exciting area for future research.

Societal Impact. We condemn the use of scene representation networks, including BACON, for ill-intentioned purposes such as malicious deepfakes or spreading misinformation, and we emphasize the importance of research to detect and thwart such efforts. See, e.g., Tewari et al. [66] for an extended discussion of strategies for mitigating misuse of neural rendering techniques.

Acknowledgments. This project was supported in part by a PECASE by the ARO and NSF award 1839974.

References

- [1] Eirikur Agustsson and Radu Timofte. Ntire 2017 challenge on single image super-resolution: Dataset and study. In *CVPR Workshops*, 2017. 3
- [2] Benjamin Attal, Selena Ling, Aaron Gokaslan, Christian Richardt, and James Tompkin. MatryODShka: Real-time 6DoF video view synthesis using multi-sphere images. In *Proc. ECCV*, 2020. 2
- [3] Matan Atzmon and Yaron Lipman. SAL: Sign agnostic learning of shapes from raw data. In *Proc. CVPR*, 2020. 2
- [4] Jonathan T. Barron, Ben Mildenhall, Matthew Tancik, Peter Hedman, Ricardo Martin-Brualla, and Pratul P. Srinivasan. Mip-NeRF: A multiscale representation for anti-aliasing neural radiance fields. In *Proc. ICCV*, 2021. 2, 5, 6
- [5] Michael Broxton, John Flynn, Ryan Overbeck, Daniel Erickson, Peter Hedman, Matthew Duvall, Jason Dourgarian, Jay Busch, Matt Whalen, and Paul Debevec. Immersive light field video with a layered mesh representation. *ACM Trans. Graph. (SIGGRAPH)*, 39(4), 2020. 2
- [6] Rohan Chabra, Jan Eric Lenssen, Eddy Ilg, Tanner Schmidt, Julian Straub, Steven Lovegrove, and Richard Newcombe. Deep local shapes: Learning local SDF priors for detailed 3D reconstruction. In *Proc. ECCV*, 2020. 2
- [7] Eric R Chan, Marco Monteiro, Petr Kellnhofer, Jiajun Wu, and Gordon Wetzstein. pi-GAN: Periodic implicit generative adversarial networks for 3D-aware image synthesis. In *Proc. CVPR*, 2021. 2
- [8] Yinbo Chen, Sifei Liu, and Xiaolong Wang. Learning continuous image representation with local implicit image function. In *Proc. CVPR*, 2021. 2
- [9] Zhiqin Chen and Hao Zhang. Learning implicit fields for generative shape modeling. In *Proc. CVPR*, 2019. 2
- [10] Zhang Chen, Yinda Zhang, Kyle Genova, Sean Fanello, Sofien Bouaziz, Christian Hane, Ruofei Du, Cem Keskin, Thomas Funkhouser, and Danhang Tang. Multiresolution deep implicit functions for 3D shape representation. In *Proc. ICCV*, 2021. 2
- [11] Eastman Kodak Company. Kodak lossless true color image suite. <http://r0k.us/graphics/kodak/>. 5
- [12] Thomas Davies, Derek Nowrouzezahrai, and Alec Jacobson. On the effectiveness of weight-encoded neural implicit 3D shapes. *arXiv preprint arXiv:2009.09808*, 2020. 2, 7
- [13] S. M. Ali Eslami, Danilo Jimenez Rezende, Frederic Besse, Fabio Viola, Ari S. Morcos, Marta Garnelo, Avraham Ruderman, Andrei A. Rusu, Ivo Danihelka, Karol Gregor, et al. Neural scene representation and rendering. *Science*, 360(6394):1204–1210, 2018. 2
- [14] Haoqiang Fan, Hao Su, and Leonidas J Guibas. A point set generation network for 3D object reconstruction from a single image. In *Proc. CVPR*, 2017. 2
- [15] Rizal Fathony, Anit Kumar Sahu, Devin Willmott, and J Zico Kolter. Multiplicative filter networks. In *Proc. ICLR*, 2020. 2, 3, 4
- [16] John Flynn, Michael Broxton, Paul Debevec, Matthew DuVall, Graham Fyffe, Ryan Overbeck, Noah Snavely, and Richard Tucker. Deepview: View synthesis with learned gradient descent. In *Proc. CVPR*, 2019. 2
- [17] Stephan J Garbin, Marek Kowalski, Matthew Johnson, Jamie Shotton, and Julien Valentin. FastNeRF: High-fidelity neural rendering at 200fps. In *Proc. ICCV*, 2021. 2
- [18] Kyle Genova, Forrester Cole, Avneesh Sud, Aaron Sarna, and Thomas Funkhouser. Local deep implicit functions for 3D shape. In *Proc. CVPR*, 2020. 2
- [19] Kyle Genova, Forrester Cole, Daniel Vlasic, Aaron Sarna, William T. Freeman, and Thomas Funkhouser. Learning shape templates with structured implicit functions. In *Proc. ICCV*, 2019. 2
- [20] Amos Gropp, Lior Yariv, Niv Haim, Matan Atzmon, and Yaron Lipman. Implicit geometric regularization for learning shapes. In *Proc. ICML*, 2020. 2
- [21] Peter Hedman, Julien Philip, True Price, Jan-Michael Frahm, George Drettakis, and Gabriel Brostow. Deep blending for free-viewpoint image-based rendering. *ACM Trans. Graph. (SIGGRAPH Asia)*, 37(6), 2018. 2
- [22] Peter Hedman, Pratul P. Srinivasan, Ben Mildenhall, Jonathan T. Barron, and Paul Debevec. Baking neural radiance fields for real-time view synthesis. In *ICCV*, 2021. 2, 6
- [23] Amir Hertz, Or Perel, Raja Giryes, Olga Sorkine-Hornung, and Daniel Cohen-Or. SAPE: Spatially-adaptive progressive encoding for neural optimization. <https://arxiv.org/abs/2104.09125>, 2021. 2
- [24] Chiyu Jiang, Avneesh Sud, Ameesh Makadia, Jingwei Huang, Matthias Nießner, and Thomas Funkhouser. Local implicit grid representations for 3D scenes. In *Proc. CVPR*, 2020. 2
- [25] Yue Jiang, Dantong Ji, Zhizhong Han, and Matthias Zwicker. SDFDiff: Differentiable rendering of signed distance fields for 3D shape optimization. In *Proc. CVPR*, 2020. 2
- [26] Tero Karras, Miika Aittala, Samuli Laine, Erik Härkönen, Janne Hellsten, Jaakko Lehtinen, and Timo Aila. Alias-free generative adversarial networks. *arXiv preprint arXiv:2106.12423*, 2021. 8
- [27] Tero Karras, Samuli Laine, and Timo Aila. A style-based generator architecture for generative adversarial networks. In *Proc. CVPR*, 2019. 8
- [28] Petr Kellnhofer, Lars Jebe, Andrew Jones, Ryan Spicer, Kari Pulli, and Gordon Wetzstein. Neural lumigraph rendering. In *CVPR*, 2021. 2
- [29] Diederik P. Kingma and Jimmy Ba. Adam: A method for stochastic optimization. *Proc. ICLR*, 2014. 5, 7
- [30] Amit Kohli, Vincent Sitzmann, and Gordon Wetzstein. Semantic implicit neural scene representations with semi-supervised training. *Proc. 3DV*, 2020. 2
- [31] David B. Lindell, Julien N. P. Martel, and Gordon Wetzstein. AutoInt: Automatic integration for fast neural volume rendering. In *Proc. CVPR*, 2021. 2
- [32] Lingjie Liu, Jiatao Gu, Kyaw Zaw Lin, Tat-Seng Chua, and Christian Theobalt. Neural sparse voxel fields. In *NeurIPS*, 2020. 2

[33] Shaohui Liu, Yinda Zhang, Songyou Peng, Boxin Shi, Marc Pollefeys, and Zhaopeng Cui. DIST: Rendering deep implicit signed distance function with differentiable sphere tracing. In *Proc. CVPR*, 2020. 2

[34] Stephen Lombardi, Tomas Simon, Jason Saragih, Gabriel Schwartz, Andreas Lehrmann, and Yaser Sheikh. Neural volumes: Learning dynamic renderable volumes from images. *ACM Trans. Graph. (SIGGRAPH)*, 38(4), 2019. 2

[35] Julien N. P. Martel, David B. Lindell, Connor Z. Lin, Eric R. Chan, Marco Monteiro, and Gordon Wetzstein. ACORN: Adaptive coordinate networks for neural scene representation. *ACM Trans. Graph. (SIGGRAPH)*, 40(4), 2021. 2

[36] Ricardo Martin-Brualla, Noha Radwan, Mehdi S. M. Sajjadi, Jonathan T. Barron, Alexey Dosovitskiy, and Daniel Duckworth. NeRF in the Wild: Neural Radiance Fields for Unconstrained Photo Collections. In *Proc. CVPR*, 2021. 2

[37] Nelson Max. Optical models for direct volume rendering. *IEEE Trans. Vis. Comput. Graph.*, 1(2):99–108, 1995. 5

[38] Lars Mescheder, Michael Oechsle, Michael Niemeyer, Sebastian Nowozin, and Andreas Geiger. Occupancy networks: Learning 3D reconstruction in function space. In *Proc. CVPR*, 2019. 1, 2, 8

[39] Mateusz Michalkiewicz, Jhony K. Pontes, Dominic Jack, Mahsa Baktashmotagh, and Anders Eriksson. Implicit surface representations as layers in neural networks. In *Proc. ICCV*, 2019. 2

[40] Ben Mildenhall, Pratul P. Srinivasan, Rodrigo Ortiz-Cayon, Nima Khademi Kalantari, Ravi Ramamoorthi, Ren Ng, and Abhishek Kar. Local light field fusion: Practical view synthesis with prescriptive sampling guidelines. *ACM Trans. Graph. (SIGGRAPH)*, 38(4), 2019. 2, 5

[41] Ben Mildenhall, Pratul P. Srinivasan, Matthew Tancik, Jonathan T. Barron, Ravi Ramamoorthi, and Ren Ng. NeRF: Representing scenes as neural radiance fields for view synthesis. In *Proc. ECCV*, 2020. 1, 2, 5, 6

[42] Thomas Neff, Pascal Stadlbauer, Mathias Panger, Andreas Kurz, Joerg H. Mueller, Chakravarty R. Alla Chaitanya, Anton S. Kaplanyan, and Markus Steinberger. DONERF: Towards Real-Time Rendering of Compact Neural Radiance Fields using Depth Oracle Networks. *Computer Graphics Forum*, 40(4), 2021. 2

[43] Michael Niemeyer and Andreas Geiger. Giraffe: Representing scenes as compositional generative neural feature fields. In *Proc. CVPR*, 2021. 2

[44] Michael Niemeyer, Lars Mescheder, Michael Oechsle, and Andreas Geiger. Occupancy flow: 4D reconstruction by learning particle dynamics. In *Proc. ICCV*, 2019. 2

[45] Michael Niemeyer, Lars Mescheder, Michael Oechsle, and Andreas Geiger. Differentiable volumetric rendering: Learning implicit 3D representations without 3D supervision. In *Proc. CVPR*, 2020. 2

[46] Michael Oechsle, Lars Mescheder, Michael Niemeyer, Thilo Strauss, and Andreas Geiger. Texture fields: Learning texture representations in function space. In *Proc. ICCV*, 2019. 2

[47] Michael Oechsle, Songyou Peng, and Andreas Geiger. UNISURF: Unifying neural implicit surfaces and radiance fields for multi-view reconstruction. In *Proc. ICCV*, 2021. 2

[48] Jeong Joon Park, Peter Florence, Julian Straub, Richard Newcombe, and Steven Lovegrove. DeepSDF: Learning continuous signed distance functions for shape representation. In *Proc. CVPR*, 2019. 1, 2

[49] Adam Paszke, Sam Gross, Francisco Massa, Adam Lerer, James Bradbury, et al. Pytorch: An imperative style, high-performance deep learning library. In *Proc. NeurIPS*, 2019. 5

[50] Songyou Peng, Chiyu Max Jiang, Yiyi Liao, Michael Niemeyer, Marc Pollefeys, and Andreas Geiger. Shape as points: A differentiable Poisson solver. In *Proc. NeurIPS*, 2021. 2

[51] Songyou Peng, Michael Niemeyer, Lars Mescheder, Marc Pollefeys, and Andreas Geiger. Convolutional occupancy networks. In *Proc. ECCV*, 2020. 2

[52] Albert Pumarola, Enric Corona, Gerard Pons-Moll, and Francesc Moreno-Noguer. D-NeRF: Neural radiance fields for dynamic scenes. In *Proc. CVPR*, 2021. 2

[53] Charles R. Qi, Hao Su, Kaichun Mo, and Leonidas J. Guibas. Pointnet: Deep learning on point sets for 3D classification and segmentation. In *Proc. CVPR*, 2017. 2

[54] Christian Reiser, Songyou Peng, Yiyi Liao, and Andreas Geiger. KiloNeRF: Speeding up neural radiance fields with thousands of tiny mlps. In *Proc. ICCV*, 2021. 2

[55] Gernot Riegler and Vladlen Koltun. Free view synthesis. In *Proc. ECCV*, 2020. 2

[56] Shunsuke Saito, Zeng Huang, Ryota Natsume, Shigeo Morishima, Angjoo Kanazawa, and Hao Li. PIFu: Pixel-aligned implicit function for high-resolution clothed human digitization. In *Proc. ICCV*, 2019. 1, 2

[57] Katja Schwarz, Yiyi Liao, Michael Niemeyer, and Andreas Geiger. GRAF: Generative radiance fields for 3D-aware image synthesis. In *Proc. NeurIPS*, 2020. 2

[58] Eero P. Simoncelli and William T. Freeman. The steerable pyramid: A flexible architecture for multi-scale derivative computation. In *Proc. ICIP*, 1995. 2

[59] Vincent Sitzmann, Eric R. Chan, Richard Tucker, Noah Snavely, and Gordon Wetzstein. MetaSDF: Meta-learning signed distance functions. In *Proc. NeurIPS*, 2020. 2

[60] Vincent Sitzmann, Julien N. P. Martel, Alexander W. Bergman, David B. Lindell, and Gordon Wetzstein. Implicit neural representations with periodic activation functions. In *Proc. NeurIPS*, 2020. 1, 2, 5, 7

[61] Vincent Sitzmann, Justus Thies, Felix Heide, Matthias Nießner, Gordon Wetzstein, and Michael Zollhöfer. DeepVoxels: Learning persistent 3D feature embeddings. In *Proc. CVPR*, 2019. 2

[62] Vincent Sitzmann, Michael Zollhöfer, and Gordon Wetzstein. Scene representation networks: Continuous 3D-structure-aware neural scene representations. In *Proc. NeurIPS*, 2019. 1, 2

[63] Pratul P. Srinivasan, Boyang Deng, Xiuming Zhang, Matthew Tancik, Ben Mildenhall, and Jonathan T. Barron. Nerv: Neural reflectance and visibility fields for relighting and view synthesis. In *CVPR*, 2021. 2

[64] Towaki Takikawa, Joey Litalien, Kangxue Yin, Karsten Kreis, Charles Loop, Derek Nowrouzezahrai, Alec Jacobson,

Morgan McGuire, and Sanja Fidler. Neural geometric level of detail: Real-time rendering with implicit 3D shapes. In *Proc. CVPR*, 2021. 2, 7

[65] Matthew Tancik, Pratul P. Srinivasan, Ben Mildenhall, Sara Fridovich-Keil, Nithin Raghavan, Utkarsh Singhal, Ravi Ramamoorthi, Jonathan T. Barron, and Ren Ng. Fourier features let networks learn high frequency functions in low dimensional domains. In *Proc. NeurIPS*, 2020. 2, 5, 7

[66] Ayush Tewari, Ohad Fried, Justus Thies, Vincent Sitzmann, Stephen Lombardi, Kalyan Sunkavalli, Ricardo Martin-Brualla, Tomas Simon, Jason Saragih, Matthias Nießner, et al. State of the art on neural rendering. *Computer Graphics Forum*, 39(2):701–727, 2020. 1, 2, 8

[67] Justus Thies, Michael Zollhöfer, and Matthias Nießner. Deferred neural rendering: Image synthesis using neural textures. *ACM Trans. Graph. (SIGGRAPH)*, 38(4):1–12, 2019. 2

[68] Antonio Torralba and Aude Oliva. Statistics of natural image categories. *Network: Computation in neural systems*, 14(3):391, 2003. 4

[69] Peng Wang, Lingjie Liu, Yuan Liu, Christian Theobalt, Taku Komura, and Wenping Wang. NeuS: Learning neural implicit surfaces by volume rendering for multi-view reconstruction. *Proc. NeurIPS*, 2021. 2

[70] Yue Wang, Yongbin Sun, Ziwei Liu, Sanjay E. Sarma, Michael M. Bronstein, and Justin M. Solomon. Dynamic graph CNN for learning on point clouds. *ACM Trans. Graph.*, 38(5):1–12, 2019. 2

[71] Lior Yariv, Jiatao Gu, Yoni Kasten, and Yaron Lipman. Volume rendering of neural implicit surfaces. *arXiv preprint arXiv:2106.12052*, 2021. 2

[72] Lior Yariv, Yoni Kasten, Dror Moran, Meirav Galun, Matan Atzmon, Ronen Basri, and Yaron Lipman. Multiview neural surface reconstruction by disentangling geometry and appearance. In *Proc. NeurIPS*, 2020. 2

[73] Wang Yifan, Lukas Rahmann, and Olga Sorkine-Hornung. Geometry-consistent neural shape representation with implicit displacement fields. *arXiv preprint arXiv:2106.05187*, 2021. 2

[74] Wang Yifan, Felice Serena, Shihao Wu, Cengiz Öztireli, and Olga Sorkine-Hornung. Differentiable surface splatting for point-based geometry processing. *ACM Trans. Graph.*, 38(6):1–14, 2019. 2

[75] Wang Yifan, Shihao Wu, Cengiz Öztireli, and Olga Sorkine-Hornung. Iso-Points: Optimizing neural implicit surfaces with hybrid representations. In *Proc. CVPR*, 2021. 2

[76] Alex Yu, Ruilong Li, Matthew Tancik, Hao Li, Ren Ng, and Angjoo Kanazawa. PlenOctrees for real-time rendering of neural radiance fields. In *ICCV*, 2021. 2

[77] Alex Yu, Vickie Ye, Matthew Tancik, and Angjoo Kanazawa. pixelNeRF: Neural radiance fields from one or few images. In *Proc. CVPR*, 2021. 2

[78] Kai Zhang, Gernot Riegler, Noah Snavely, and Vladlen Koltun. Nerf++: Analyzing and improving neural radiance fields. *arXiv preprint arXiv:2010.07492*, 2020. 2

[79] Xiuming Zhang, Sean Fanello, Yun-Ta Tsai, Tiancheng Sun, Tianfan Xue, Rohit Pandey, Sergio Orts-Escolano, Philip Davidson, Christoph Rhemann, Paul Debevec, Jonathan T. Barron, Ravi Ramamoorthi, and William T. Freeman. Neural light transport for relighting and view synthesis. *ACM Trans. Graph.*, 40(1), 2021. 2

[80] Tinghui Zhou, Richard Tucker, John Flynn, Graham Fyffe, and Noah Snavely. Stereo magnification: Learning view synthesis using multiplane images. *ACM Trans. Graph. (SIGGRAPH)*, 37(4), 2018. 2

BACON: Band-limited Coordinate Networks for Multiscale Scene Representation

Supplemental Material

David B. Lindell Dave Van Veen Jeong Joon Park Gordon Wetzstein
Stanford University

<http://computationalimaging.org/publications/bacon>

Contents

1. Supplemental Derivations	2
1.1. Deriving the Number of Sines	2
1.2. Deriving the Distribution of Frequencies	3
1.3. Initialization and Distribution of Activations	6
1.3.1 Preliminary Derivations	6
1.3.2 Proof of the Initialization Scheme	7
1.3.3 Empirical Evaluation	8
2. Supplemental Results	10
2.1. Images	10
2.2. Neural Radiance Fields	13
2.2.1 Additional Implementation Details	13
2.2.2 Supplemental Results	13
2.3. 3D Shape Representation	17
2.3.1 Additional Implementation Details	17
2.3.2 Supplemental Results	17
2.4. Accelerated Marching Cubes	24
2.4.1 Adaptive-Frequency SDF Evaluation	24
2.4.2 Multi-scale SDF Evaluation	24
2.4.3 Combining the Two Strategies	24
2.4.4 Discussion of Occupancy Networks	24
2.5. Comparison to Explicit Fourier Basis	27

1. Supplemental Derivations

1.1. Deriving the Number of Sines

Lemma 1.1.1. *The product of two sines is the sum of two sines with frequencies corresponding to the sum and difference of the initial frequencies.*

$$\sin(\omega_1 x + \phi_1) \cdot \sin(\omega_2 x + \phi_2) = \frac{1}{2} \left[\sin((\omega_1 + \omega_2) \cdot x + \phi_1 + \phi_2 - \pi/2) + \sin((\omega_1 - \omega_2) \cdot x + \phi_1 - \phi_2 + \pi/2) \right] \quad (1)$$

Proof. Without loss of generality, let $\sin(a) = \sin(\omega_1 x + \phi_1)$ and $\sin(b) = \sin(\omega_2 x + \phi_2)$. Then,

$$\sin(a) \cdot \sin(b) = \frac{e^{ja} - e^{-ja}}{2j} \cdot \frac{e^{jb} - e^{-jb}}{2j} \quad (2)$$

$$= \frac{e^{j(a+b)} + e^{-j(a+b)} - e^{j(a-b)} - e^{-j(a-b)}}{-4} \quad (3)$$

$$= -\frac{1}{2} \frac{e^{-j\pi/2}}{-j} \frac{e^{j(a+b)} + e^{-j(a+b)}}{2} + \frac{1}{2} \frac{e^{j\pi/2}}{j} \frac{e^{j(a-b)} + e^{-j(a-b)}}{2} \quad (4)$$

$$= \frac{1}{2} \frac{e^{j(a+b-\pi/2)} + e^{-j(a+b-\pi/2)-j\pi}}{2j} + \frac{1}{2} \frac{e^{j(a-b+\pi/2)} + e^{-j(a-b+\pi/2)+j\pi}}{2j} \quad (5)$$

$$= \frac{1}{2} \frac{e^{j(a+b-\pi/2)} - e^{-j(a+b-\pi/2)}}{2j} + \frac{1}{2} \frac{e^{j(a-b+\pi/2)} - e^{-j(a-b+\pi/2)}}{2j} \quad (6)$$

$$= \frac{1}{2} \left[\sin(a + b - \pi/2) + \sin(a - b + \pi/2) \right] \quad (7)$$

(8)

□

Theorem 1.1.1. *The number of sines represented by a multiplicative filter network is given as*

$$N_{\text{sine}}^{(N_L)} = \sum_{i=0}^{N_L-1} 2^i d_h^{i+1},$$

where N_L is the number of layers and d_h is the number of hidden features in the network.

Proof. Consider a $N_L = 1$ layer network, given as

$$\mathbf{z}_0 = \sin(\boldsymbol{\omega}_0 \mathbf{x} + \boldsymbol{\phi}_0) \quad (9)$$

This expression is a vector of sines, and the proof follows trivially for $N_L = 1$; the number of sines represented by this network is exactly d_h because we have $\mathbf{x} \in \mathbb{R}^{d_{\text{in}}}$ and $\boldsymbol{\omega}_0 \in \mathbb{R}^{d_h \times d_{\text{in}}}$.

To build intuition, we also analyze the case of $N_L = 2$, which gives

$$\mathbf{z}_1 = \sin(\boldsymbol{\omega}_1 \mathbf{x} + \boldsymbol{\phi}_1) \circ [\mathbf{W}_1 \sin(\boldsymbol{\omega}_0 \mathbf{x} + \boldsymbol{\phi}_0) + \mathbf{b}_1] \quad (10)$$

$$= \sin(\boldsymbol{\omega}_1 \mathbf{x} + \boldsymbol{\phi}_1) \circ [\mathbf{W}_1 \sin(\boldsymbol{\omega}_0 \mathbf{x} + \boldsymbol{\phi}_0)] + \sin(\boldsymbol{\omega}_1 \mathbf{x} + \boldsymbol{\phi}_1) \circ \mathbf{b}_1 \quad (11)$$

(12)

where

$$\sin(\boldsymbol{\omega}_1 \mathbf{x} + \boldsymbol{\phi}_1) \circ [\mathbf{W}_1 \sin(\boldsymbol{\omega}_0 \mathbf{x} + \boldsymbol{\phi}_0)] \quad (13)$$

$$= \begin{bmatrix} \sin(\boldsymbol{\omega}_1^{(1)} \mathbf{x} + \boldsymbol{\phi}_1^{(1)}) \\ \vdots \\ \sin(\boldsymbol{\omega}_1^{(d_h)} \mathbf{x} + \boldsymbol{\phi}_1^{(d_h)}) \end{bmatrix} \circ \begin{bmatrix} W_1^{(1,1)} \sin(\boldsymbol{\omega}_0^{(1)} \mathbf{x} + \boldsymbol{\phi}_0^{(1)}) + \cdots + W_1^{(1,d_h)} \sin(\boldsymbol{\omega}_0^{(d_h)} \mathbf{x} + \boldsymbol{\phi}_0^{(d_h)}) \\ \vdots \\ W_1^{(d_h,1)} \sin(\boldsymbol{\omega}_0^{(1)} \mathbf{x} + \boldsymbol{\phi}_0^{(1)}) + \cdots + W_1^{(d_h,d_h)} \sin(\boldsymbol{\omega}_0^{(d_h)} \mathbf{x} + \boldsymbol{\phi}_0^{(d_h)}). \end{bmatrix} \quad (14)$$

Given that the Hadamard product between each row in the above expression results in a doubling of the number of sines (**Lemma 1.1.1**), the entire Hadamard product results in a vector containing $2d_h^2$ sines. The remaining term $\sin(\omega_1 \mathbf{x} + \phi_1) \circ \mathbf{b}_1$ contributes an additional d_h sines, for a total $2d_h^2 + d_h$ sines in the $N_L = 2$ layer network. In general, the linear component \mathbf{W}_i of each layer multiplies the total number of sines by d_h and the Hadamard product with the sine doubles this by a factor of 2. An additional d_h sines are contributed by the bias term.

Now, assume we have a network with $N_L = k$ layers. Let $L_i(\mathbf{z}) = \mathbf{W}_i \mathbf{z} + \mathbf{b}_i$ and let $g_i(\mathbf{x}) = \sin(\omega_i \mathbf{x} + \phi_i)$. Then we have

$$\mathbf{z}_{k-1} = g_{k-1}(\mathbf{x}) \circ (L_{k-1}(g_{k-2}(\mathbf{x}) \circ (\dots (g_2(\mathbf{x}) \circ (\underbrace{(L_2(g_1(\mathbf{x}) \circ (\underbrace{(L_1 g_0(\mathbf{x})))) \dots))}_{d_h}) \dots))), \quad (15)$$

where the brackets indicate the number of sines for successive terms, revealing the following recursion for the number of sines in each layer.

$$N_{\text{sine}}^{(1)} = d_{\text{h}} \quad (16)$$

$$N_{\text{sine}}^{(i+1)} = d_{\text{h}} + 2d_{\text{h}}N_{\text{sine}}^{(i)} \quad (17)$$

To complete a proof by induction let us assume that the theorem holds for $N_L = k$, and we have

$$N_{\text{sine}}^{(k+1)} = d_{\text{h}} + 2d_{\text{h}}N_{\text{sine}}^{(k)} \quad (18)$$

$$= d_h + 2d_h \sum_{i=0}^{k-1} 2^i d_h^{i+1} \quad (19)$$

$$= d_h + \sum_{i=0}^{k-1} 2^{i+1} d_h^{i+2} \quad \text{let } j = i + 1. \quad (20)$$

$$= d_h + \sum_{j=1}^k 2^j d_h^{j+1} \quad (21)$$

$$= \sum_{i=0}^k 2^j d_h^{j+1} \quad (22)$$

which is the original result, completing the proof. \square

Corollary 1.1.1. *If we remove the bias layers from each L_i , then we remove the additional of d_h from the recursion and it becomes*

$$\tilde{N}_{\text{sine}}^{(1)} = d_h \quad (23)$$

$$\tilde{N}_{\text{sine}}^{(i+1)} = 2d_h N_{\text{sine}}^{(i)}, \quad (24)$$

such that

$$\tilde{N}_{\text{sine}}^{(N_{\text{L}})} = 2^{N_{\text{L}}-1} d_b^{N_{\text{L}}}. \quad (25)$$

1.2. Deriving the Distribution of Frequencies

Lemma 1.2.1. Let X_i , $i = 1, 2, \dots$ be a sequence of independent, identically distributed random variables. Then, let N be a discrete random variable that is independent of X_i and takes on values $N > 0$. Now, define the compound random variable

$$S_N = \sum_{i=0}^{N-1} X_i, \quad (26)$$

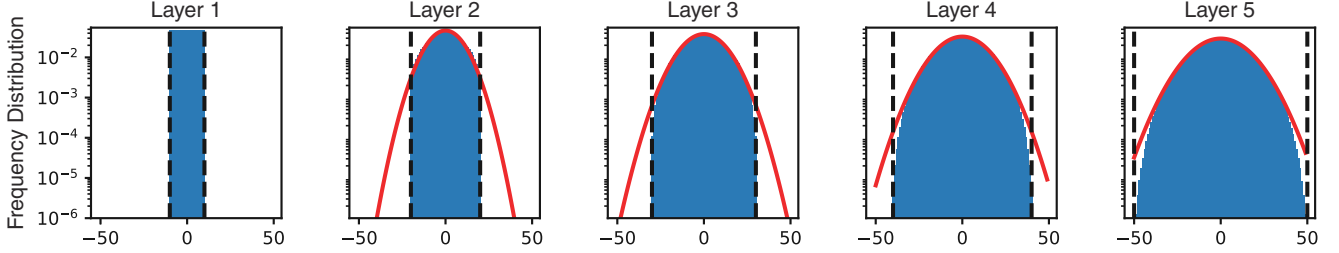


Figure 1. Empirical evaluation of distribution of frequencies. We plot the distribution of frequencies at the output of each layer in a 5-layer network with hidden features $d_h = 1024$ bandwidth B_i equal to 10 (averaged over 1000 network realizations). The output of the first layer is uniformly distributed and successive layers increasingly approximate the normal distribution according to the Central Limit Theorem. A normal distribution with variance calculated using **Theorem 1.2.1** is plotted in red and closely matches the observed distribution.

The variance of S_N is given by

$$\text{Var}(S_N) = E[N] \text{Var}(X_1) + \text{Var}(N)E[X_1]^2 \quad (27)$$

Proof. The proof follows from the law of total variance (see, e.g., p. 286 of Chatfield and Theobald [4]). \square

Lemma 1.2.2. *Central Limit Theorem.* Let X_1, \dots, X_n be a sequence of independent and identically distributed random variables with finite mean and variance, μ and σ^2 , respectively, and let $S_n = \sum_{i=1}^n X_i$. For large n , S_n approximates the normal distribution with $E[S_n] = n\mu$ and $\text{Var}(S_n) = n\sigma^2$

Proof. See Ash et al. [2]. \square

Theorem 1.2.1. *The frequencies of BACON are approximately Gaussian distributed with variance equal to*

$$\left[\sum_{m=0}^{N_L-1} m \cdot \frac{2^{N_L-1-m} d_h^{N_L-m}}{\sum_{i=0}^{N_L-1} 2^i d_h^{i+1}} \right] \cdot \text{Var}(\omega_i^{(j_i)}). \quad (28)$$

where $\text{Var}(\omega_i^{(j_i)})$ is the variance of the initialized frequencies in each input sine layer g_i .

Proof. The overall idea is that, if the number of sines is in the network is given as $\sum_{i=0}^{N_L-1} 2^i d_h^{i+1}$ (**Theorem 1.1.1**), then it turns out that the i th element in this sum describes the number of sines whose frequency is the sum of $i+1$ random variables. Then, we can use **Lemma 1.2.1** and **Lemma 1.2.2** to derive the variance and distribution of the network frequencies.

First, let us show that the frequency of each sine represented by the network is itself a sum of random variables. We write an expression for the number of sines in the network $F_i(\omega)$ at frequency ω directly after applying the Hadamard product with $g_i(\mathbf{x})$. Let $\delta(\omega)$ represent the Dirac delta function. Expanding on our previous results, we have that

$$F_0(\omega) = \int_{-\infty}^{\infty} \underbrace{\sum_{j=0}^{d_h-1} \delta(\omega - \omega_0^{(j)})}_{f_0(\omega)} d\omega. \quad (29)$$

This expression simply places a delta function at the location of each frequency and the integral checks to see how many frequencies exist at the input parameter frequency, ω .

Now, recall the previous result that adding the next layer multiplies the number of frequencies by $2d_h$ and adds an additional d_h frequencies. We use the convolution operator $*$ to shift the frequencies of the previous layer according to

Lemma 1.1.1. The additional d_h frequencies result from the multiplication of the sine layer and the bias term from the previous layer. Thus we can give the following expression for the frequencies at layer $i + 1$.

$$F_{i+1}(\omega) = \int_{-\infty}^{\infty} f_i(\omega) * \underbrace{\sum_{j=0}^{d_h-1} [\delta(\omega - \omega_{i+1}^{(j)}) + \delta(\omega + \omega_{i+1}^{(j)})]}_{\text{shifts spectrum according to Lemma 1.1.1}} + \underbrace{\sum_{j=0}^{d_h-1} \delta(\omega - \omega_{i+1}^{(j)})}_{\text{new frequencies from the bias term}} \, d\omega. \quad (30)$$

If we ignore frequencies resulting from the bias terms in the above expression, we would have that there are $2^{N_L-1} d_h^{N_L}$ sines in an N_L layer network (**Theorem 1.1.1**) with output frequencies given as

$$\bar{\omega} = \omega_0^{(j_0)} + s_1 \omega_1^{(j_1)} + \cdots + s_{N_L-1} \omega_{N_L-1}^{(j_{N_L-1})} \quad (31)$$

for some $s_0, \dots, s_{N_L-1} \in \{-1, 1\}$ and indices $j_0, \dots, j_{N_L-1} \in \{0, 1, \dots, d_h - 1\}$. Including the bias term at the i th layer (for $i > 0$) simply results in an additional $2^{N_L-1-i} d_h^{N_L-i}$ sines in the network, whose frequencies are a sum of $N_L - i$ terms (corresponding exactly to the terms of the sum in **Theorem 1.1.1**). Thus, frequencies represented by the network are drawn from a compound distribution (as in **Lemma 1.2.1**) since they can be the sum of from 1 to N_L random variables.

Now we can describe the distribution of the frequencies of the network. Let the variance of an element of ω_i be given by $\text{Var}(\omega_i^{(j_i)})$. Then, the output frequency $\bar{\omega}$ is a compound random variable such that

$$\bar{\omega} = \omega_M^{(j_M)} + \sum_{i=M+1}^{N_L-1} s_i \omega_i^{(j_i)} \quad M \in \{0, \dots, N_L - 1\} \quad (32)$$

and M is a random variable whose probability depends on the total number of frequencies in the network that contribute to each possible value of M . Specifically, using **Theorem 1.1.1** to evaluate the fraction of sines for each value of M gives

$$p_M(m) = \frac{2^{N_L-1-m} d_h^{N_L-m}}{\sum_{i=0}^{N_L-1} 2^i d_h^{i+1}}. \quad (33)$$

We can calculate the resulting variance using the law of total variance outlined in **Lemma 1.2.1**.

$$\text{Var}(\bar{\omega}) = E[M] \text{Var}(\omega_i^{(j_i)}) + \text{Var}(M) E[\omega_i^{(j_i)}]^2 \quad (34)$$

$$= E[M] \text{Var}(\omega_i^{(j_i)}) \quad \omega_i^{(j_i)} \text{ zero mean} \quad (35)$$

$$= \sum_{m=0}^{N_L-1} m \cdot p_M(m) \text{Var}(\omega_i^{(j_i)}) \quad (36)$$

$$= \left[\sum_{m=0}^{N_L-1} m \cdot \frac{2^{N_L-1-m} d_h^{N_L-m}}{\sum_{i=0}^{N_L-1} 2^i d_h^{i+1}} \right] \cdot \text{Var}(\omega_i^{(j_i)}) \quad (37)$$

Finally, we note that $\bar{\omega}$ becomes the sum of a large number of random variables as the number of hidden layers in the network increases, and so we can approximate the distribution as a Gaussian using the Central Limit Theorem (**Lemma 1.2.2**). We show that this holds empirically in Fig. 1, where we show the simulated distribution of frequencies in each layer of a 5-layer network with $d_h = 1024$ and $B_i = 10$, averaged over 1000 realizations. The distribution of frequencies is well-approximated by a Gaussian with the derived variance (especially for increasing layers). \square

1.3. Initialization and Distribution of Activations

1.3.1 Preliminary Derivations

Lemma 1.3.1. *Let X and Y be two independent random variables with probability density functions f_X and f_Y . Then the probability density function $f_Z(z)$ of $Z = XY$ is given as*

$$f_Z(z) = \int_{-\infty}^{\infty} f_X(x) f_Y(z/x) \frac{1}{|x|} dx. \quad (38)$$

Proof. See Grimmett and Stirzaker [7]. \square

Theorem 1.3.1. *Let W , X , and P be independent random variables sampled from continuous uniform distributions as*

$$W \sim \mathcal{U}(-B, B) \quad (39)$$

$$X \sim \mathcal{U}(-0.5, 0.5) \quad (40)$$

$$P \sim \mathcal{U}(-\pi, \pi) \quad (41)$$

where $B \gg \pi$. Then let $Z = WX + P$. The probability density function $f_Z(z)$ of Z is approximately

$$f_Z(z) \approx \begin{cases} \frac{1}{B} \log\left(\frac{B}{|2z|}\right), & -B/2 \leq z \leq B/2 \\ 0, & \text{else} \end{cases}. \quad (42)$$

Proof. Let $\tilde{Z} = WX$. Then, $f_{\tilde{Z}}(z)$ is given as (Lemma 1.3.1):

$$f_{\tilde{Z}}(z) = \int_{-\infty}^{\infty} f_W(w) f_X(z/w) \frac{1}{|w|} dw \quad (43)$$

$$= 2 \int_0^{\infty} f_W(w) f_X(z/w) \frac{1}{w} dw \quad (44)$$

$$= \frac{1}{B} \int_0^B f_X(z/w) \frac{1}{w} dw \quad (45)$$

$$f_X(z/w) = \begin{cases} 1 & -0.5 \leq z/w \leq 0.5 \\ 0 & \text{else} \end{cases} \quad (46)$$

$$= \begin{cases} 1 & w \leq -2z, w \geq 2z \\ 0 & \text{else} \end{cases} \quad (47)$$

$$= \frac{1}{B} \int_{\min(2z, B)}^B \frac{1}{w} dw \quad (48)$$

$$= \frac{1}{B} \log(|w|) \Big|_{\min(2z, B)}^B \quad (49)$$

$$= \frac{1}{B} \log\left(\frac{B}{\min(|2z|, B)}\right) \quad (50)$$

$$= \begin{cases} \frac{1}{B} \log\left(\frac{B}{|2z|}\right), & -B/2 \leq z \leq B/2 \\ 0, & \text{else} \end{cases} \quad (51)$$

Now, $Z = WX + P = \tilde{Z} + P$ and $f_Z = f_{\tilde{Z}} * f_P$, where $*$ indicates convolution. For $B \gg \pi$, the support of f_P is sufficiently small that we can neglect the “broadening” effect of the convolution, such that $f_Z \approx f_{\tilde{Z}}$. \square

Theorem 1.3.2. With Z and B as defined in **Theorem 1.3.1**, we have that

$$\text{Var}[\sin(Z)] \approx \frac{1}{2} \left[1 - \frac{\text{SI}(B)}{B} \right] \approx \frac{1}{2} \quad (52)$$

Proof.

$$\text{Var}[\sin(Z)] = \mathbb{E}[\sin^2(Z)] \quad (53)$$

$$= \frac{1}{2}(1 - \mathbb{E}[\cos(2Z)]) \quad (54)$$

$$\mathbb{E}[\cos(2Z)] = \int_{-\infty}^{\infty} f_Z(z) \cos(2z) dz \quad (55)$$

$$\approx \frac{1}{B} \int_{-B/2}^{B/2} \log\left(\frac{B}{|2z|}\right) \cos(2z) dz \quad (\text{Theorem 1.3.1}) \quad (56)$$

$$\text{Integrate by parts: } \int f dg = fg - \int df g \quad (57)$$

$$f = \log\left(\frac{B}{|2z|}\right), dg = \cos(2z) dz, df = -\frac{1}{z} dz, g = \frac{1}{2} \sin(2z) \quad (58)$$

$$= \frac{1}{B} \left[\frac{1}{2} \log\left(\frac{B}{|2z|}\right) \sin(2z) + \underbrace{\int \frac{\sin(2z)}{2z} dz}_{\frac{1}{2} \text{SI}(2z)} \right]_{-B/2}^{B/2} \quad (59)$$

$$= \frac{1}{2B} \left[\log\left(\frac{B}{|2z|}\right) \sin(2z) + \text{SI}(2z) \right]_{-B/2}^{B/2} \quad (60)$$

$$= \frac{1}{2B} \left[\log\left(\frac{B}{|2z|}\right) \sin(2z) + \text{SI}(2z) \right]_{-B/2}^{B/2} \quad (61)$$

$$= \frac{\text{SI}(B)}{B} \approx \frac{\pi}{2B}, B \gg 0 \quad (62)$$

$$\Rightarrow \frac{1}{2}(1 - \mathbb{E}[\cos(2Z)]) = \frac{1}{2} \left(1 - \frac{\text{SI}(B)}{B} \right) \quad (63)$$

$$\approx \frac{1}{2} \left(1 - \frac{\pi}{2B} \right), B \gg 0 \quad (64)$$

$$\approx \frac{1}{2} \quad (65)$$

Where we used that $\text{SI}(x)$ is the sine integral function: $\text{SI}(x) = \int_0^x \frac{\sin(t)}{t} dt$. \square

Lemma 1.3.2. The variance of the product of two random variables X and Y is given by

$$\text{Var}[X \cdot Y] = \text{Var}[X] \cdot \text{Var}[Y] + \mathbb{E}[Y]^2 \cdot \text{Var}[X] + \mathbb{E}[X]^2 \cdot \text{Var}[Y] \quad (66)$$

Proof. Refer to Goodman [6]. \square

1.3.2 Proof of the Initialization Scheme

Theorem 1.3.3. Let the input to BACON be uniformly distributed in $[-0.5, 0.5]$ and the frequency ω_i of each layer be uniformly distributed in $[-B_i, B_i]$ with $B_i \gg 0$. Then, let the linear layer weights \mathbf{W}_i applied after the sine layers be distributed according to a random uniform distribution in the interval $[-\sqrt{6/d_h}, \sqrt{6/d_h}]$. The activations after each linear layer are standard normal distributed.

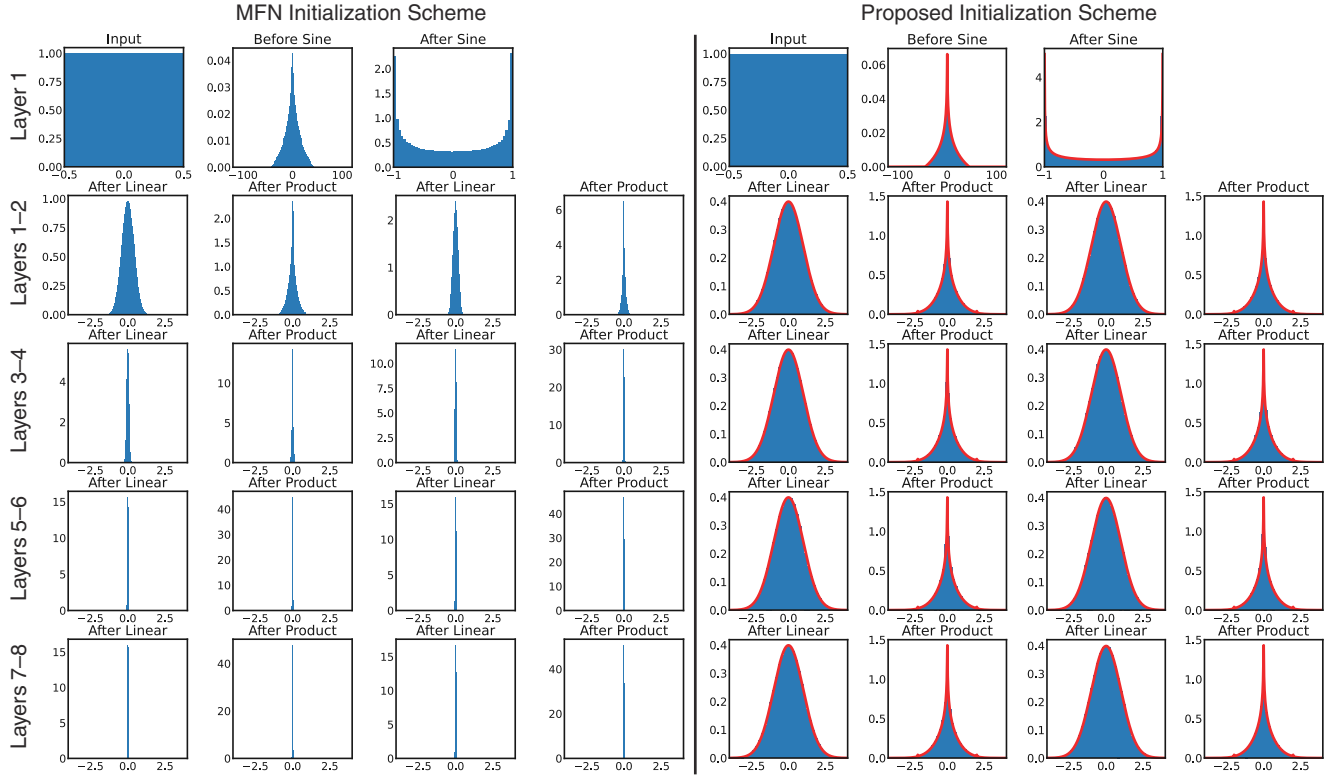


Figure 2. Empirical evaluation of initialization scheme. We show the default MFN initialization scheme (left) [5], and the proposed initialization scheme (right) for a network with 9 sine layers and 1024 hidden features (d_h). For our method we set the bandwidth B_i of each layer to an arbitrary value of 30π . We use the default settings of the MFN codebase, which initializes the linear layers \mathbf{W}_i uniformly in $[-\sqrt{256/d_h}, \sqrt{256/d_h}]$ and sets the bandwidth to $B_i = 256\sqrt{d_{in}}$. Note that the proposed initialization scheme resolves the issue of the activation magnitude becoming extremely small with increased network depth. We also show that the distribution of activations closely matches our derivations, with the analytical expressions plotted in red.

Proof. A sketch of the proof is as follows.

- The variance of the output of each sine layer $g_i(\mathbf{x})$ is approximately 0.5 (**Theorem 1.3.2**).
- The output after applying the first linear layer $\mathbf{W}_1 g_0(\mathbf{x})$ is standard normal distributed (neglecting the effect of the bias). We have that the i th output is $\sum_{j=0}^{d_h-1} \mathbf{W}_1^{(i,j)} g_0(\mathbf{x})^{(j)}$, with $\text{Var}(\mathbf{W}_1^{(i,j)} g_0(\mathbf{x})^{(j)}) = \text{Var}(\mathbf{W}_1^{(i,j)}) \cdot \text{Var}(g_0(\mathbf{x})^{(j)}) = \frac{1}{12} (2\sqrt{6/d_h})^2 \cdot \frac{1}{2} = 1/d_h$ (**Lemma 1.3.2**). Then the entire sum has variance $d_h \cdot 1/d_h = 1$, and is normal distributed by the Central Limit Theorem (**Lemma 1.2.2**).
- The output of the Hadamard product $g_1(\mathbf{x}) \circ (\mathbf{W}_1 g_0(\mathbf{x}) + \mathbf{b}_1)$ has variance $\text{Var}(g_1(\mathbf{x})) \cdot \text{Var}(\mathbf{W}_1 g_0(\mathbf{x}) + \mathbf{b}_1) \approx \frac{1}{2} \cdot 1 = \frac{1}{2}$ (**Lemma 1.3.2**).
- The distribution after applying the next linear layer \mathbf{W}_{i+1} is again standard normal (using the same steps of taking the product of the variances and applying the Central Limit Theorem), and the same steps as above can be repeated to show the distributions are standard normal after each linear layer.

□

1.3.3 Empirical Evaluation

We empirically evaluate the initialization scheme and derivations by showing plots of the distributions of activations for BACON with 9 sine layers, 1024 hidden features (d_h), and an arbitrary bandwidth $B_i = 30\pi$. The plot is shown in Fig. 2, and

we overlay the analytical expression for the distribution at each intermediate output of the network. We also compare to the conventional MFN initialization proposed by Fathony et al. [5] using the publicly available implementation¹. Their proposed method initializes the linear layers \mathbf{W}_i to a random uniform value in $[-\sqrt{256/d_h}, \sqrt{256/d_h}]$ and sets the bandwidth to $B_i = 256\sqrt{d_{in}}$. We find that this causes the magnitude of the activations to decrease significantly with increasing network size, leading to vanishing gradients. There are five different distributions that can be observed at intermediate outputs of the network with our proposed initialization scheme:

1. The input to the network is uniformly distributed in [-0.5, 0.5].
2. The output of the linear layers applied directly to the input (that is, $\omega_i \mathbf{x} + \phi_i$) is distributed as derived in **Theorem 1.3.1**.
3. We find empirically that the output of $g_i(\mathbf{x}) = \sin(\omega_i \mathbf{x} + \phi_i)$ is approximately arcsine distributed and the variance is approximately 1/2 as derived in **Theorem 1.3.2**. In Fig. 2, we show the empirical distribution together with a plot of the arcsine distribution with support over $[-1, 1]$ given by the probability density function $f_X(x) = \frac{1}{\pi\sqrt{1-x^2}}$. Note the close correspondence of the arcsine distribution and the observed histogram of activations in Fig. 2. We believe the connection to the arcsine distribution is related to previous work, which shows that the sine of uniform and normal random variables are both approximately arcsine distributed [10].
4. The output of $\mathbf{W}_1 g_0(\mathbf{x}) + \mathbf{b}_1$ is standard normal distribution as described in **Theorem 1.3.3**. Also, the outputs of other linear layers \mathbf{W}_i with bias \mathbf{b}_i are standard normal distributed.
5. The output of the Hadamard product $g_i(\mathbf{x}) \circ (\mathbf{W}_i \mathbf{z}_{i-1} + \mathbf{b}_i)$ is the product of an (approximately) arcsine distribution and a standard normal distribution. The distribution of a product of random variables is described by **Lemma 1.3.1**, and the variance of this distribution is approximately equal to 1/2 (**Lemma 1.3.2**). We numerically calculate the probability density function for the product of a standard normal and arcsine distribution according to **Lemma 1.3.1** and find that this approximates the empirical distribution as shown in Fig. 2.

¹<https://github.com/boschresearch/multiplicative-filter-networks>

2. Supplemental Results

2.1. Images

We evaluate BACON on an image fitting task and compare its performance to three other methods: a ReLU network using Gaussian Fourier Features positional encoding (PE) [12] and SIREN [10], both supervised at 256×256 ($1 \times$) resolution, and a ReLU network using integrated PE (adapted from Mip-NeRF) [3] with supervision at $1/4$, $1/2$, and $1 \times$ resolutions. BACON is supervised at a single scale ($1 \times$) and learns a multiscale decomposition. All networks contain 4 hidden layers with 256 hidden features and are trained as described in the main text.

Figure 3 shows all output resolutions ($1/4$, $1/2$, 1 , and $4 \times$) for the result shown in the main text. Figure 4 shows additional results on center-cropped images from the DIV2K dataset [1]. In all results, Fourier Features and SIREN fit to a single scale and show aliasing when subsampled, i.e. at $1/4$ and $1/2$ resolution. Integrated PE learns reasonable anti-aliasing as it is explicitly supervised on anti-aliased pixel values. The band-limited nature of BACON allows it to closely represent a low-pass filtered image while only explicitly supervising at $1 \times$ resolution. At $4 \times$ resolution, all methods except BACON show high-frequency artifacts.

We perform a quantitative evaluation of the image fitting performance by training on a dataset of 16 randomly selected images from the DIV2K dataset and reporting the peak signal to noise ratio (PSNR) and structural similarity index measure (SSIM). We resize center crops of the images to 512×512 resolution and then fit a model to a subsampled grid of 256×256 pixels for each image. We evaluate the performance on this training set of pixels as well as an offset validation grid of 256×256 pixels. Quantitative results in Table 1 demonstrate that all methods fit the training set to well over 30dB PSNR at 256×256 ($1 \times$) resolution. All methods perform similarly on the validation set. Remarkably, BACON demonstrates similar performance to the single-scale representations while simultaneously representing all output scales.

# Params.		Training		Validation	
		PSNR	SSIM	PSNR	SSIM
Fourier Features	264K	37.362 ± 2.544	0.976 ± 0.009	27.574 ± 1.861	0.896 ± 0.036
SIREN	265K	41.851 ± 2.084	0.987 ± 0.006	27.448 ± 2.022	0.907 ± 0.034
Integrated PE	274K	33.092 ± 2.219	0.930 ± 0.027	26.138 ± 1.789	0.835 ± 0.052
BACON	268K	38.871 ± 1.727	0.979 ± 0.005	27.424 ± 1.752	0.900 ± 0.024

Table 1. Quantitative evaluation (mean \pm standard deviation) for image fitting. Methods are trained on a grid of 256×256 pixels subsampled from a 512×512 image. Metrics are reported on this training dataset for all methods (for BACON and Integrated Positional Encoding we compare to the highest resolution output). We also report the validation performance on an offset grid of 256×256 pixels, where all methods perform similarly. Remarkably, BACON achieves comparable training and validation performance to the single-scale baselines while simultaneously representing multiple output scales.

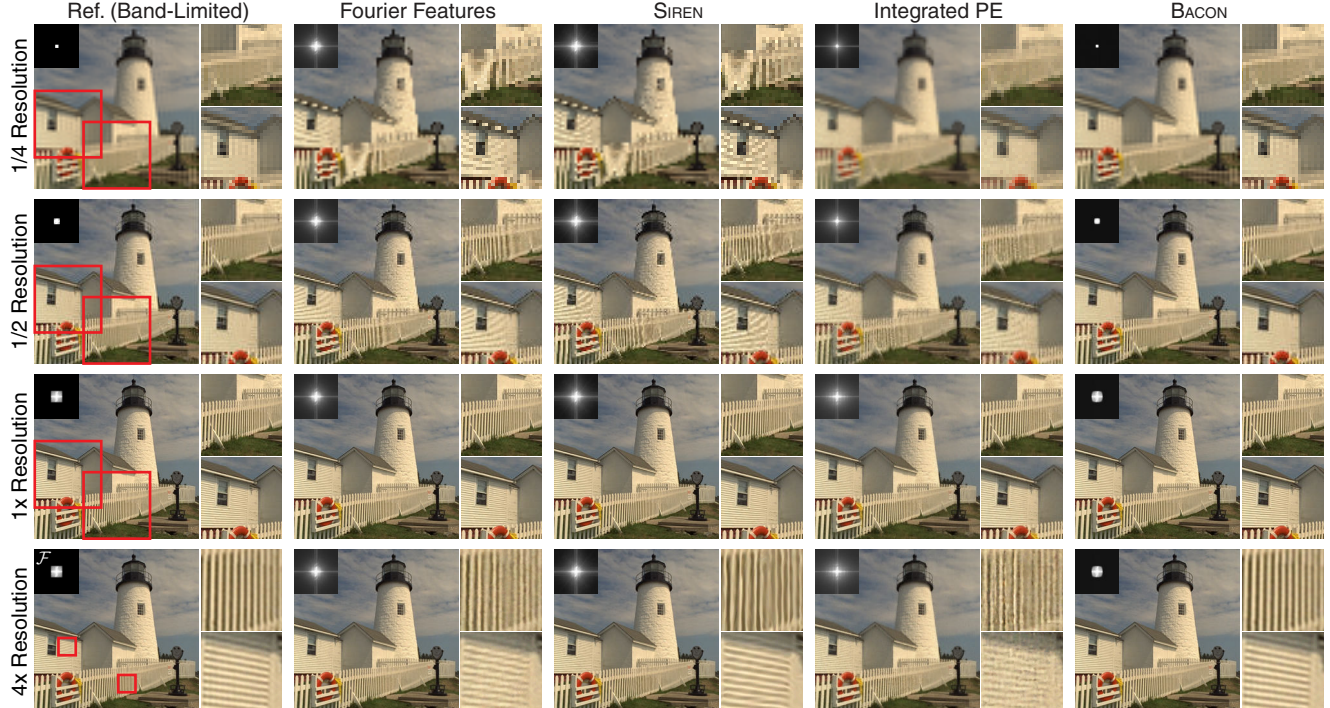


Figure 3. Image fitting results. We train a ReLU network using Fourier features (FF) positional encoding (PE) [12] and a SIREN [10] to fit an image at 256×256 ($1\times$) resolution, and evaluate the models at 64×64 ($1/4$), 128×128 ($1/2$), 256×256 ($1\times$), and 1024×1024 ($4\times$) resolution. Since these methods fit to a single scale, we see aliasing at lower resolutions, and high-frequency artifacts at $4\times$ resolution (see insets). We train a ReLU network with integrated PE [3] with supervision at $1/4$, $1/2$, and $1\times$ resolutions. While this network learns anti-aliasing at low resolutions, inference at the unsupervised $4\times$ resolution yields artifacts. Finally, BACON is supervised at a single scale, learning band-limited outputs that closely match a low-pass filtered reference image (see left column, and Fourier spectra insets). All methods achieve an accurate fit at $1\times$ resolution with PSNRs of 37.838 dB (FF PE), 41.513 dB (SIREN), 34.105 dB (Integrated PE), and 40.314 dB (BACON).

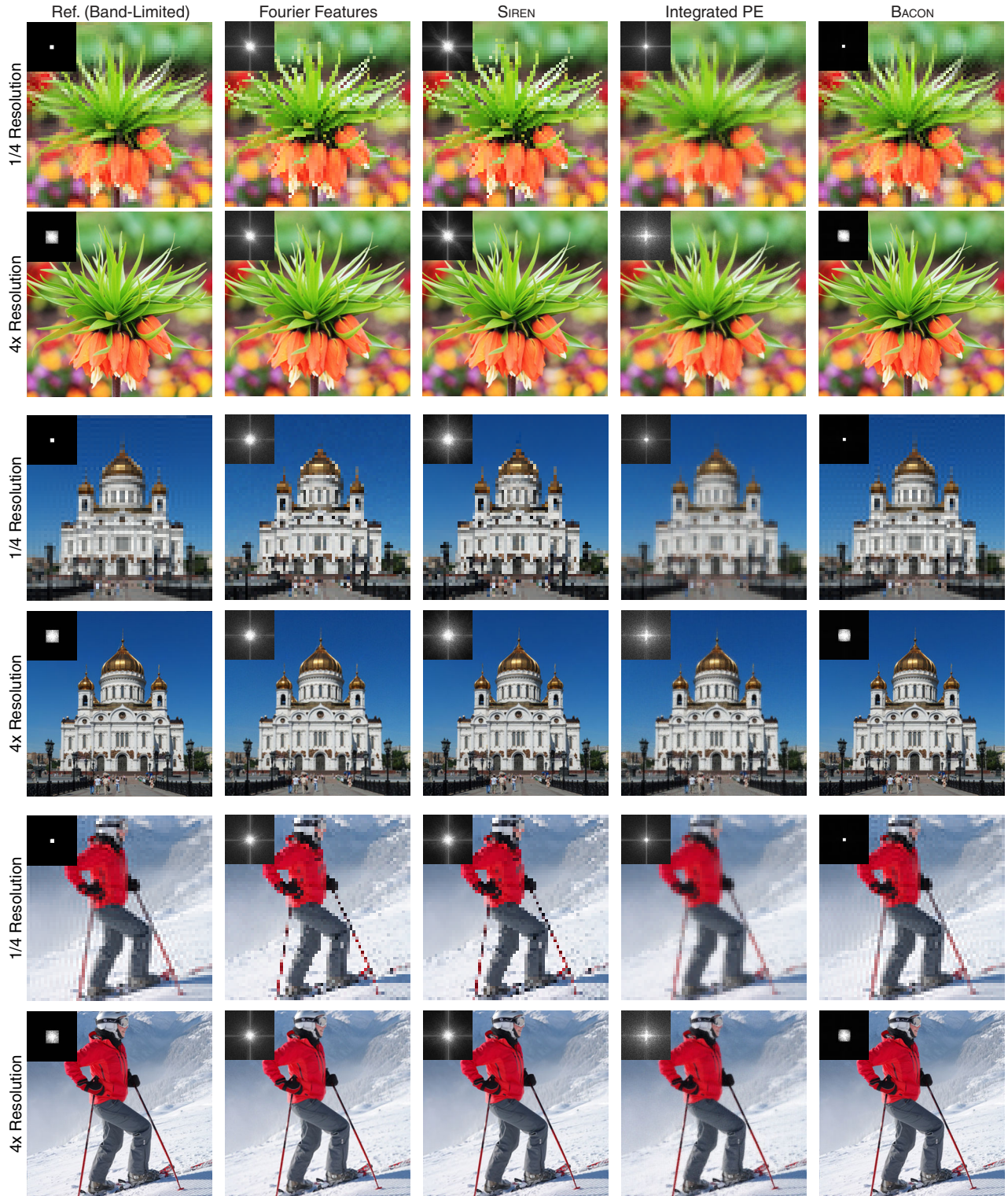


Figure 4. Supplemental image fitting results. We show the output of baseline methods and BACON fit to a subset of images from the DIV2K dataset. Similar to previous results, we observe aliasing in baseline methods when subsampling to lower resolutions, and artifacts in $4\times$ supersampled outputs. BACON produces anti-aliased outputs at low-resolution and interpretable upsampled results via band-limited interpolation.

2.2. Neural Radiance Fields

We provide additional implementation details and results on reconstructing neural radiance fields using NeRF [9], Mip-NeRF [3], and BACON.

2.2.1 Additional Implementation Details

For training neural radiance fields, we use BACON with 8 hidden layers and 256 hidden features. We set the bandwidth of each layer using random uniform initialization with $\omega_i \sim \mathcal{U}(-B_i, B_i)$. For a maximum bandwidth B , we set $B_0 = B_1 = B_2 = B/24$, $B_3 = B_4 = B/16$, $B_5 = B_6 = 1/8$, and $B_7 = B_8 = 1/4$ such that $\sum_{i=0}^8 B_i = B$.

For training BACON we also adopt the regularization strategy of Hedman et al. [8] to penalize non-zero off-surface opacity values, σ . We include this term to mitigate non-zero opacity at unsupervised locations can produce hazy spots in the rendered images using BACON. The regularization penalty is given as

$$\mathcal{L}_{\text{reg}} = \lambda_\sigma \sum_{i,j,k} \log \left(1 + 2\sigma_k(\mathbf{r}_i, \mathbf{t}_j^f) \right), \quad (67)$$

where λ_σ is a weight that we decay from logarithmically from 1e-3 to 1e-6 during training.

Additionally, we find that we can obtain a roughly 30% speedup for training and inference without noticeable drop in performance by re-using outputs g_i throughout the network. For example, for layers where $B_i = B_{i+1}$, we set $g_i = g_{i+1}$, allowing us to reuse computation and reducing the number of input layers that need to be computed by roughly half.

2.2.2 Supplemental Results

In Tables 2 and 3 we provide the per-scene average PSNR and SSIM for each method. We observe the same trends as in the main paper, with Mip-NeRF achieving the best performance, while BACON outperforms NeRF and uses a fraction of the parameters to render the low-resolution outputs compared to either baseline. Additional qualitative results are shown in Fig. 5, where we show output images for each scene at each scale. Finally, we show additional results for learning neural radiance fields in a semi-supervised case in Fig. 6. Here, outputs of BACON at each scale are supervised on full resolution images, and BACON automatically learns the multiscale decomposition of the neural radiance field used for rendering.

		PSNR									
# Params.		chair	drums	ficus	hotdog	lego	materials	mic	ship	Avg.	
NeRF	511K	28.767	24.025	25.188	29.685	26.539	24.758	26.720	26.028	26.464	
		33.064	25.492	26.161	33.478	30.782	26.618	30.615	28.163	29.297	
		32.882	24.503	25.387	33.711	31.037	25.850	30.517	27.640	28.941	
		29.565	22.741	24.280	31.408	28.228	24.319	27.827	25.508	26.734	
		31.070	24.190	25.254	32.071	29.147	25.386	28.920	26.834	27.859	
Mip-NeRF	511K	37.174	28.200	28.177	37.332	33.924	30.414	35.803	31.631	32.832	
		36.700	26.979	26.951	37.131	34.266	29.233	34.977	30.503	32.093	
		35.724	25.560	26.685	36.622	34.295	27.972	34.219	29.379	31.307	
		33.374	24.005	26.428	34.984	33.136	26.764	32.494	27.808	29.874	
		35.743	26.186	27.060	36.517	33.905	28.596	34.373	29.830	31.526	
BACON	329K	31.764	25.967	27.184	31.670	29.161	25.899	28.609	27.549	28.475	
		32.523	26.094	25.562	32.175	29.768	25.268	29.524	27.244	28.520	
		31.958	25.074	24.319	32.342	29.890	24.948	29.444	26.552	28.066	
		30.729	24.175	23.753	31.942	30.418	24.300	28.454	25.668	27.430	
		31.744	25.327	25.204	32.032	29.809	25.104	29.008	26.753	<u>28.123</u>	

Table 2. PSNR for each method averaged over each scene of the multiscale Blender dataset.

# Params.		SSIM								Avg.
		chair	drums	ficus	hotdog	lego	materials	mic	ship	
NeRF 1/8		0.941	0.902	0.918	0.957	0.930	0.944	0.963	0.876	0.929
NeRF 1/4		0.976	0.926	0.947	0.973	0.968	0.943	0.980	0.888	0.950
NeRF 1/2	511K	0.972	0.909	0.942	0.968	0.961	0.922	0.971	0.865	0.939
NeRF 1×		0.935	0.879	0.925	0.951	0.922	0.895	0.947	0.820	0.909
NeRF Avg.		0.956	0.904	0.933	0.962	0.945	0.926	0.965	0.862	0.932
Mip-NeRF 1/8		0.990	0.952	0.951	0.986	0.984	0.978	0.994	0.928	0.970
Mip-NeRF 1/4		0.989	0.942	0.954	0.983	0.984	0.964	0.990	0.909	0.964
Mip-NeRF 1/2	511K	0.986	0.929	0.960	0.980	0.982	0.949	0.985	0.890	0.957
Mip-NeRF 1×		0.975	0.915	0.957	0.973	0.972	0.932	0.980	0.861	0.946
Mip-NeRF Avg.		0.985	0.935	0.955	0.981	0.980	0.955	0.987	0.897	0.959
BACON 1/8	133K	0.962	0.919	0.933	0.967	0.954	0.945	0.970	0.882	0.942
BACON 1/4	266K	0.972	0.931	0.930	0.966	0.948	0.922	0.975	0.877	0.940
BACON 1/2	398K	0.968	0.923	0.927	0.965	0.949	0.913	0.968	0.854	0.934
BACON 1×	531K	0.957	0.917	0.926	0.959	0.951	0.901	0.958	0.827	0.924
BACON Avg.	329K	0.965	0.923	0.929	0.964	0.951	0.921	0.968	0.860	<u>0.935</u>

Table 3. SSIM for each method averaged over each scene of the multiscale Blender dataset.



Figure 5. Neural radiance field results. Outputs of NeRF [9], Mip-NeRF [3], and BACON are shown, where all outputs are supervised using each scale of the multiscale Blender dataset.

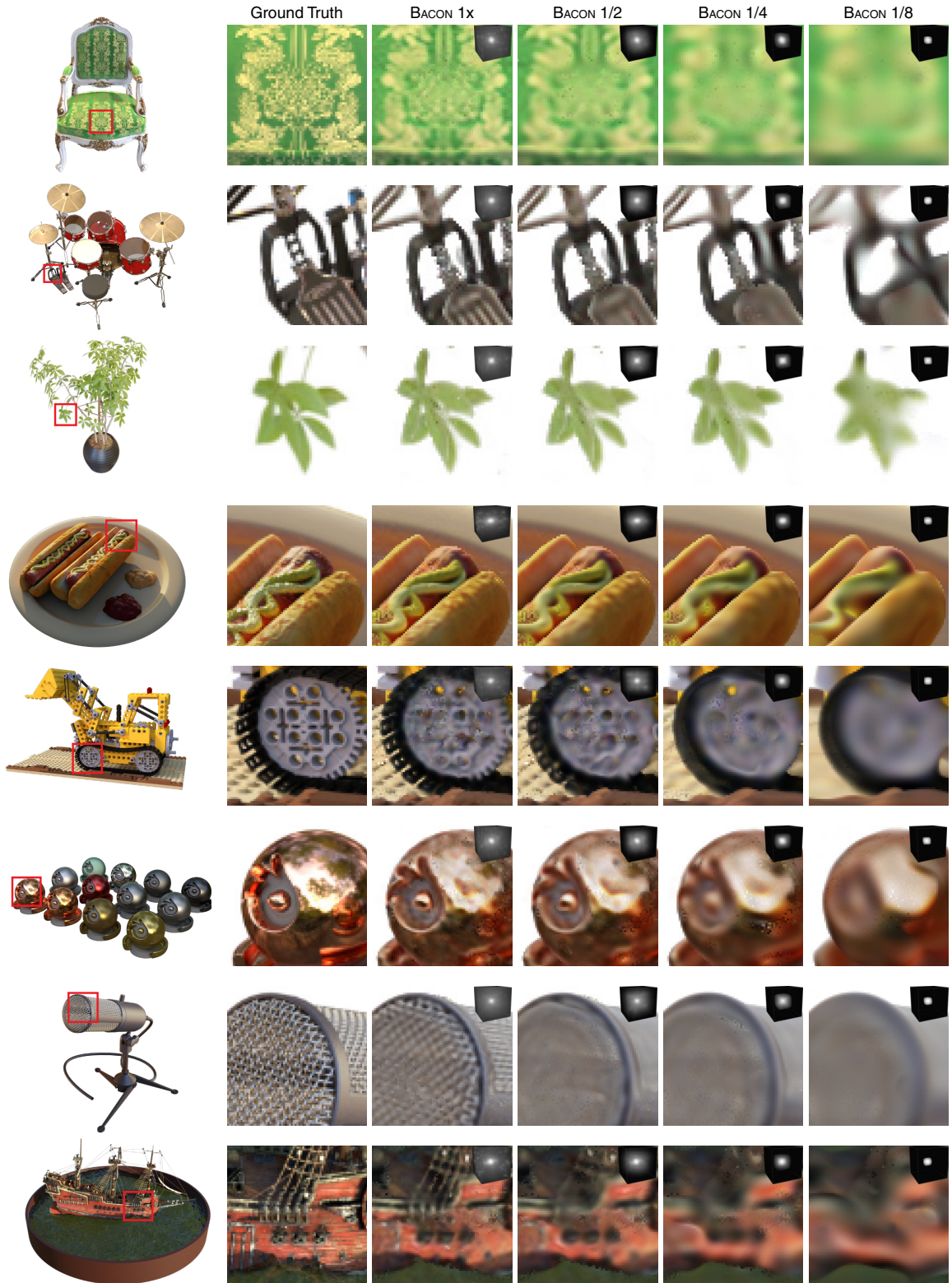


Figure 6. Results of training BACON with all outputs supervised at high resolution. BACON learns a multiscale decomposition for each scene. Fourier spectra of the learned opacity volume are shown as insets.

2.3. 3D Shape Representation

2.3.1 Additional Implementation Details

We evaluate BACON on 3D shape representation with SDFs and compare its performance to three other methods: Fourier Features [12], SIREN [10], and Neural Geometric Level of Detail (NGLOD) [11]. All networks are trained to directly fit a signed distance function estimated from a ground-truth mesh. For BACON, Fourier Features, and SIREN we use 8 hidden layers with 256 hidden features. We scale the shape models so that they fit within a volume whose dimensions extend from -0.5 to 0.5. The maximum bandwidth of BACON is set to 256 cycles per unit interval for the *Lucy* and *Thai Statue* scenes, and to 192 cycle per unit interval for the *Armadillo*, *Dragon*, and *Sphere* models. We scale the bandwidth of each layer the same as with the neural radiance field models as described in the main text. We determine the maximum bandwidth empirically such that the network achieves a good fit to high frequency details in the model with noticeable smoothing in the lower levels of detail.

After training, the models are extracted at 512^3 resolution using marching cubes, and we evaluate performance using Chamfer distance and intersection over union (IOU). Chamfer distance is calculated by sampling 300,000 points on the surface of the ground truth and predicted models and then finding the distance to the closest point on the other surface. That is, for the two point clouds P_1 , and P_2 we compute

$$D_{\text{Chamfer}}(P_1, P_2) = \frac{1}{|P_1|} \sum_{\mathbf{x} \in P_1} \min_{\mathbf{y} \in P_2} \|\mathbf{x} - \mathbf{y}\|_2^2 + \frac{1}{|P_2|} \sum_{\mathbf{y} \in P_2} \min_{\mathbf{x} \in P_1} \|\mathbf{x} - \mathbf{y}\|_2^2. \quad (68)$$

For the IOU score, we compute intersection and union of the occupancy values for the ground truth and predicted meshes on a 128^3 grid of points centered on the object.

2.3.2 Supplemental Results

We include shape fitting results for four scenes from the Stanford 3D Scanning Repository (*Armadillo*, *Dragon*, *Lucy*, *Thai Statue*) and a simple sphere in Figures 7, 8, 9, 10, and 11. All methods perform similarly at the highest level of detail (see Table 4). For lower levels of detail, BACON (1/8, 1/4, 1/2) represents a smooth multiscale decomposition of the shape, while the representations for NGLOD (NGLOD-1,2,3) show angular artifacts due to their high-frequency spectra (see figure insets). Note that results for NGLOD are shown for training the representation on a maximum of 4 levels of detail (i.e., the number of trained levels of their feature octree) and then rendering out the resulting trained levels of detail 1–4.

Table 4 includes quantitative evaluation of each method for the *Armadillo*, *Dragon*, *Lucy*, *Thai Statue* scenes, and a simple sphere baseline (with radius 0.25). The highest detail outputs of all methods perform comparably, including BACON, which achieves similar performance despite simultaneously representing multiple levels of detail. NGLOD generally improves at higher levels of detail at the cost of significantly more model parameters. Here, NGLOD 1–4 represent outputs from the model trained at maximum level of detail 4, and we also train separate models with maximum levels of detail 5–6 (NGLOD-5 and NGLOD-6).

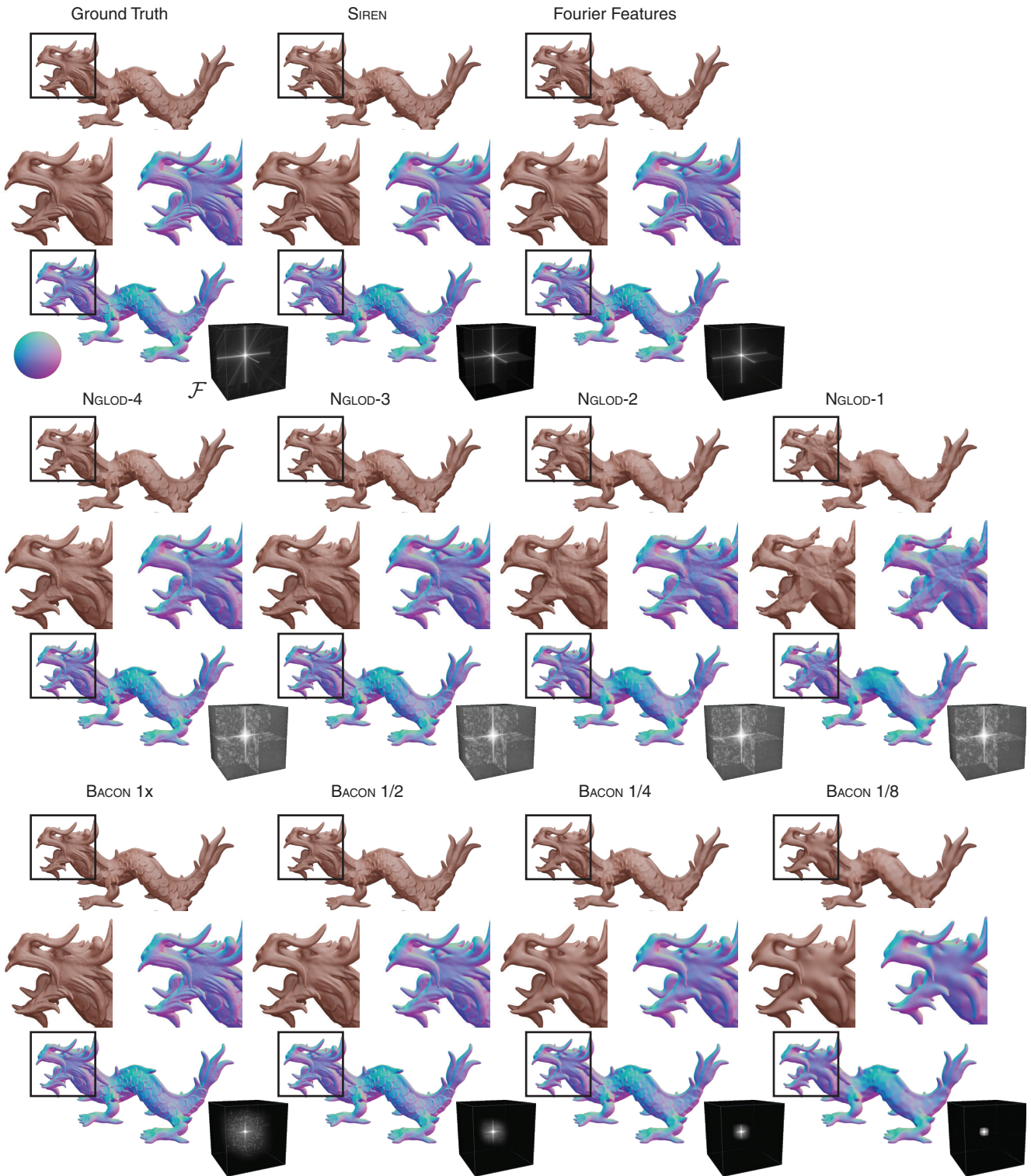
Additionally, Table 5 includes evaluation of shape fitting at lower levels of detail for BACON and NGLOD (trained with a maximum level of detail 4). Note that here NGLOD has fewer parameters than BACON for lower levels of detail; this is not true for the full resolution models, as number of parameters scales superlinearly for NGLOD and linearly for BACON.

Parameters	Sphere		Dragon		Armadillo		Lucy		Thai Statue		
	Chamfer \downarrow	IOU \uparrow									
Fourier Features	527K	8.364e-7	1.000e+0	1.861e-6	9.828e-1	3.230e-6	9.897e-1	2.956e-6	9.654e-1	1.946e-6	9.823e-1
SIREN	528K	8.407e-7	1.000e+0	2.762e-6	9.621e-1	3.895e-6	9.858e-1	3.706e-6	9.625e-1	2.695e-6	9.651e-1
NGLOD-4	1.35M	9.722e-7	9.990e-1	2.272e-6	9.722e-1	3.410e-6	9.891e-1	5.479e-6	9.421e-1	2.320e-6	9.689e-1
NGLOD-5	10.1M	9.443e-7	<u>9.993e-1</u>	2.211e-6	9.841e-1	3.804e-6	9.835e-1	3.206e-6	9.621e-1	2.047e-6	9.767e-1
NGLOD-6	78.8M	1.064e-6	9.966e-1	1.918e-6	<u>9.840e-1</u>	3.212e-6	9.911e-1	<u>3.013e-6</u>	9.634e-1	<u>1.939e-6</u>	9.824e-1
BACON 1 \times	531K	8.353e-7	1.000e+0	<u>1.875e-6</u>	9.831e-1	3.233e-6	9.893e-1	3.075e-6	<u>9.650e-1</u>	1.972e-6	9.791e-1

Table 4. Quantitative evaluation of 3D shape fitting for high-detail outputs. All methods show comparable performance. Neural Geometric Level of Detail (NGLOD) [11] is shown for levels of detail 4, 5, and 6 and performance generally increases (as does the model parameter count) with increasing levels of detail. BACON gives comparable performance at the highest resolution scale to other methods despite simultaneously representing multiple levels of detail.

Parameters	Sphere		Dragon		Armadillo		Lucy		Thai Statue		
	Chamfer↓	IOU↑	Chamfer↓	IOU↑	Chamfer↓	IOU↑	Chamfer↓	IOU↑	Chamfer↓	IOU↑	
NGLOD-1	8.74K	9.391e-7	9.987e-1	6.624e-6	9.381e-1	6.435e-6	9.699e-1	1.965e-5	8.936e-1	8.139e-6	9.392e-1
NGLOD-2	36.8K	9.549e-7	9.989e-1	3.247e-6	9.612e-1	4.033e-6	9.839e-1	7.550e-6	9.288e-1	3.474e-6	9.638e-1
NGLOD-3	199K	1.100e-6	9.975e-1	2.274e-6	9.722e-1	3.407e-6	9.891e-1	5.513e-6	9.421e-1	2.325e-6	9.689e-1
BACON 1/8	133K	8.349e-7	1.000e+0	3.430e-6	9.624e-1	3.997e-6	9.844e-1	5.309e-6	9.461e-1	3.168e-6	9.622e-1
BACON 1/4	266K	8.320e-7	1.000e+0	<u>2.223e-6</u>	<u>9.773e-1</u>	<u>3.355e-6</u>	<u>9.892e-1</u>	<u>3.467e-6</u>	<u>9.627e-1</u>	<u>2.119e-6</u>	<u>9.748e-1</u>
BACON 1/2	398K	<u>8.343e-7</u>	1.000e+0	1.955e-6	9.815e-1	3.242e-6	9.897e-1	3.174e-6	9.652e-1	1.985e-6	9.799e-1

Table 5. Quantitative evaluation of 3D shape fitting for BACON and Neural Geometric Level of Detail (NGLOD) [11] for low levels of detail. Here, NGLOD has fewer parameters than BACON, and BACON generally achieves better performance.



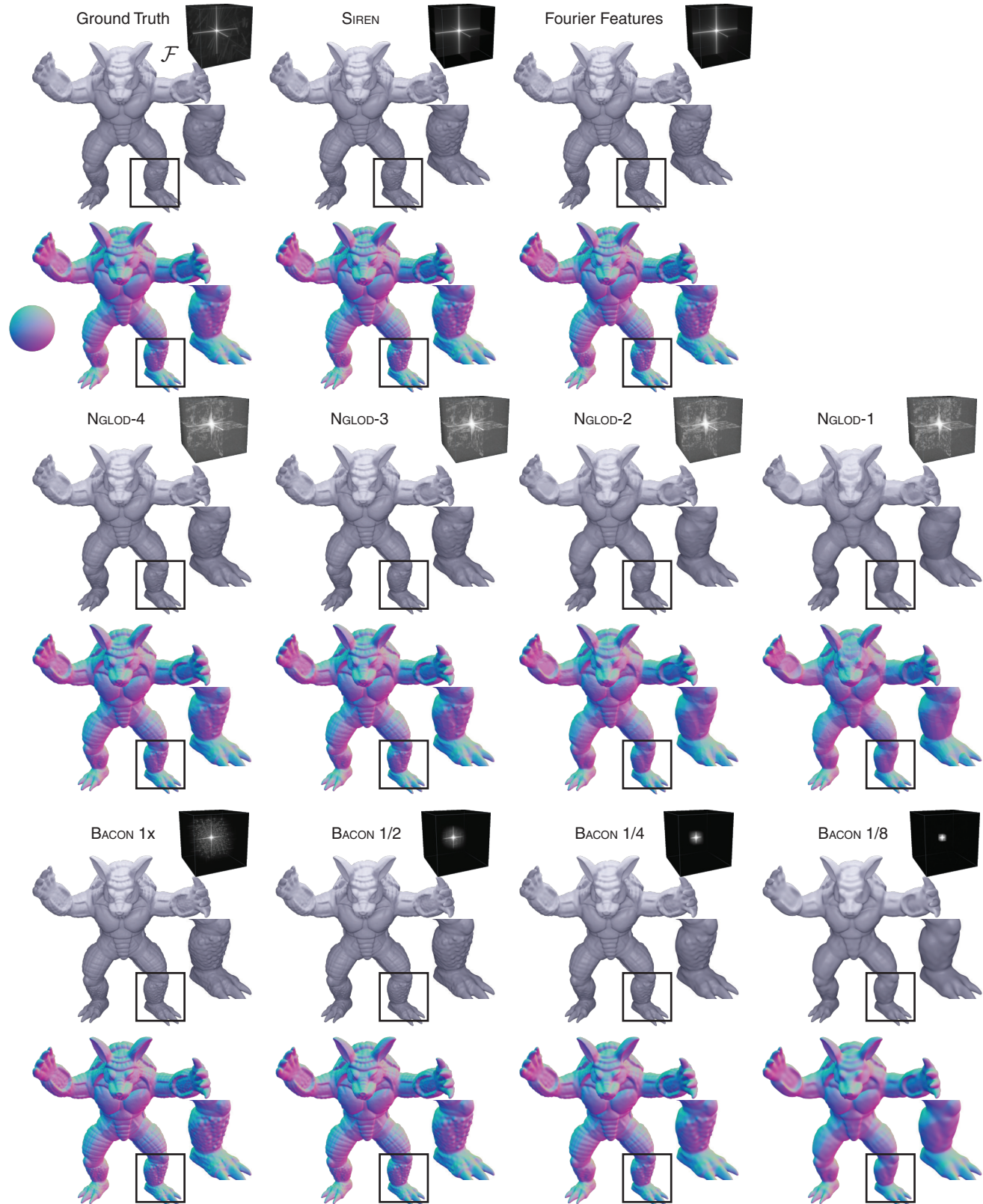


Figure 8. Qualitative results on the *Armadillo* scene. Rendered objects and normal maps are shown, and Fourier spectra of the SDF values are included as insets.

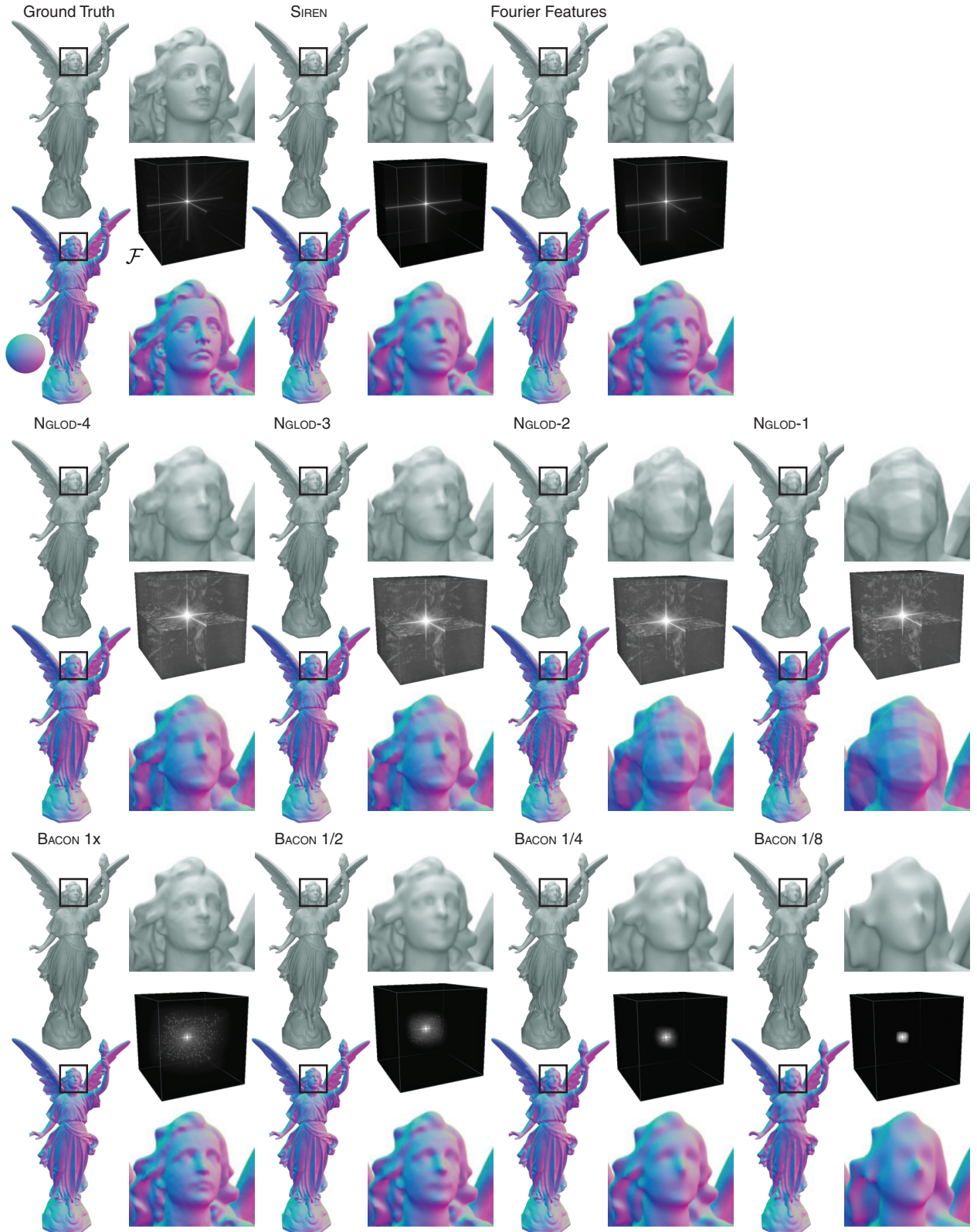


Figure 9. Qualitative results on the *Lucy* scene. Rendered objects and normal maps are shown, and Fourier spectra of the SDF values are included as insets.

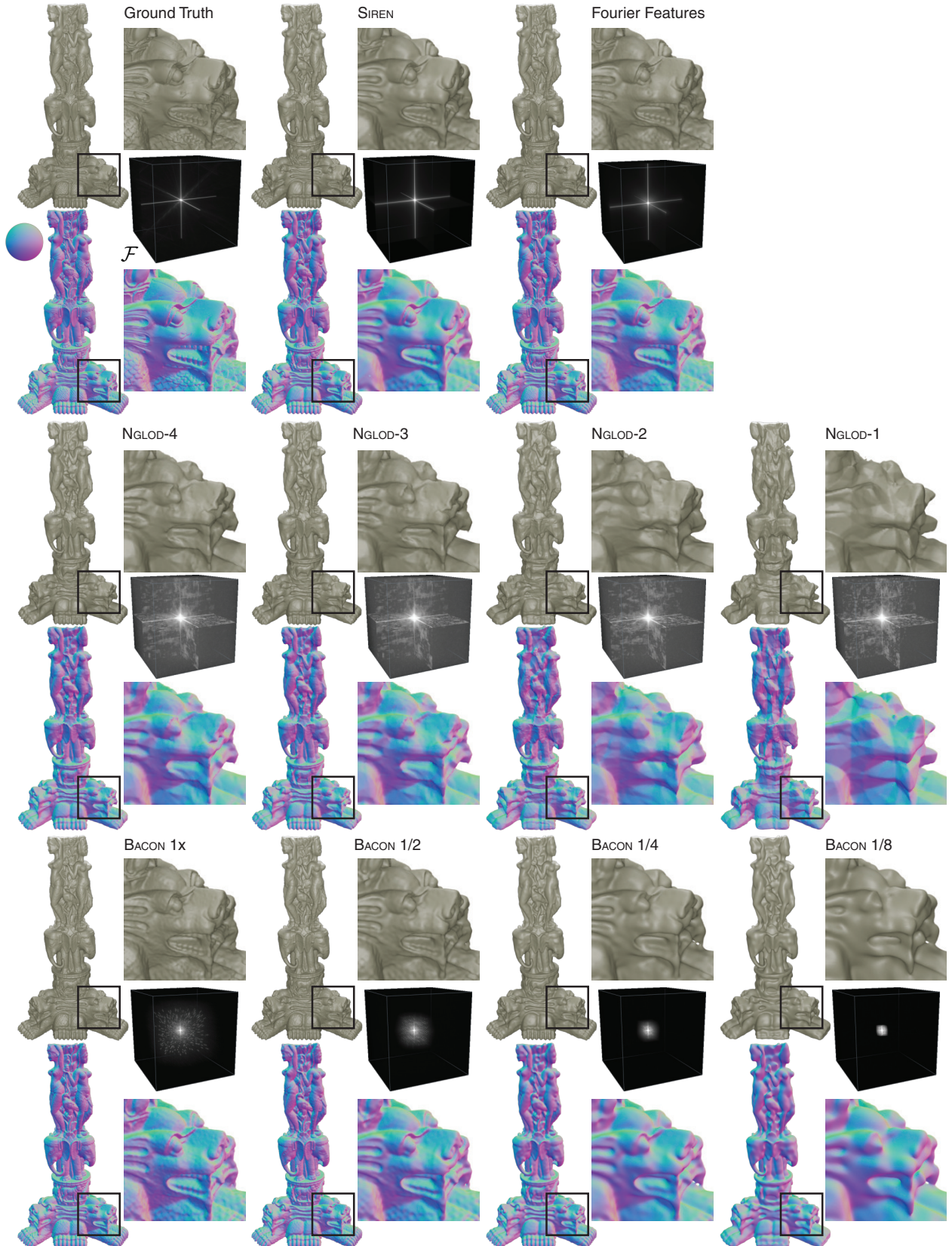


Figure 10. Qualitative results on the *Thai Statue* scene. Rendered objects and normal maps are shown, and Fourier spectra of the SDF values are included as insets.

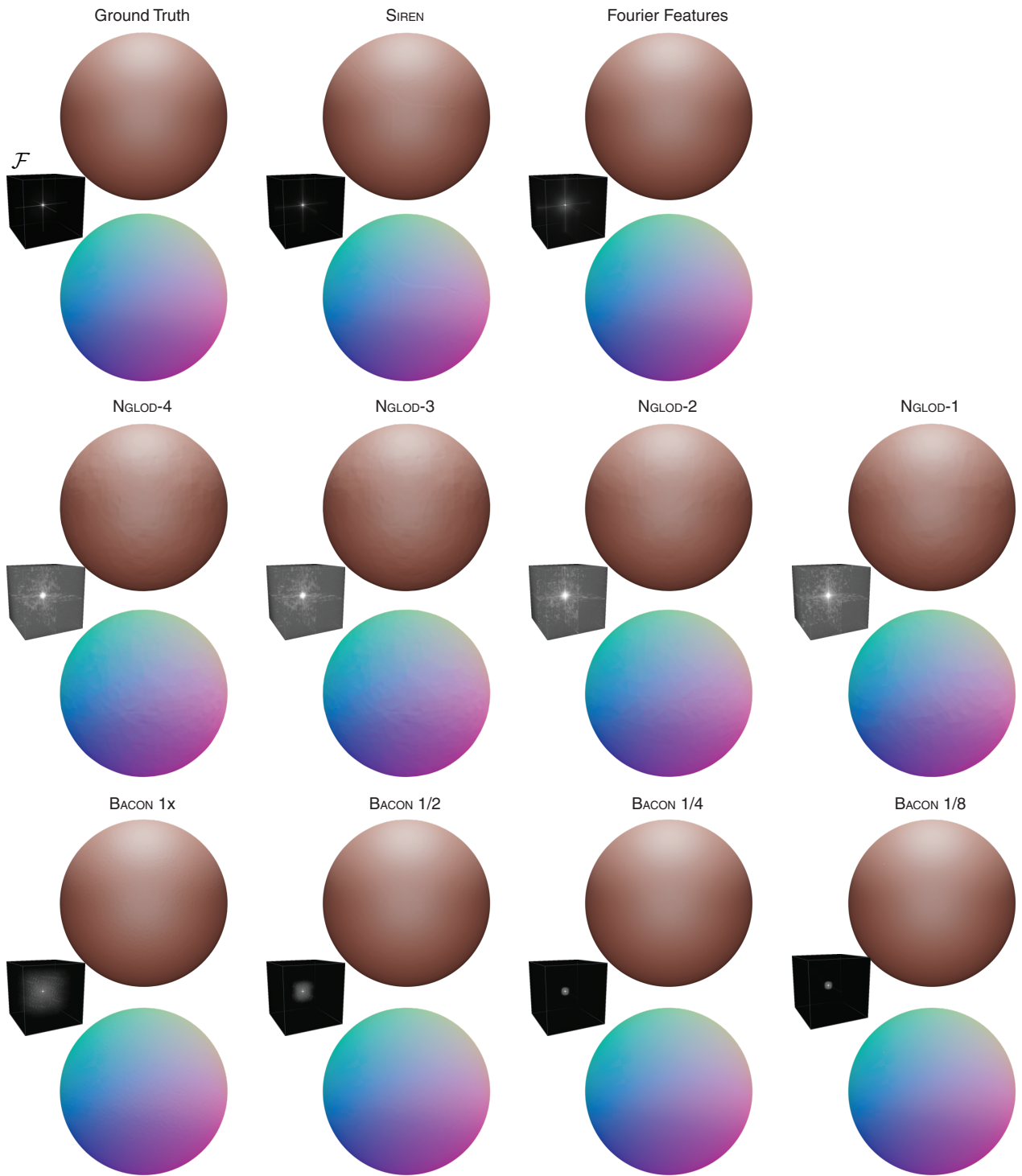


Figure 11. Qualitative results on the *Sphere* scene. Rendered objects and normal maps are shown, and Fourier spectra of the SDF values are included as insets.

2.4. Accelerated Marching Cubes

In this section, we explain two strategies for accelerating mesh extraction via the Marching Cubes algorithm with signed distance function (SDF) representation networks.

2.4.1 Adaptive-Frequency SDF Evaluation

We observe that the band-limited, multi-scale nature of our network allows efficient allocation of computational resources when evaluating SDFs. The key idea is to adaptively choose whether to use SDFs from low-frequency or high-frequency output layers (Fig. 12). For each cell, we compute the low-frequency output SDF_{low} that takes a fraction of time of the full network evaluation. Then, for cells that are far away from the zero-level-set (i.e., magnitude of SDF_{low} larger than some threshold τ), we adopt early-stopping and do not proceed to the higher network layers, as we do not need highly-accurate SDFs for empty cells. For cells near the surface (i.e., $|SDF_{low}| < \tau$), we need accurate SDFs, and thus we use the full network for high-frequency outputs. This adaptive early-stopping strategy meaningfully reduces the computation time for mesh extraction (Table 6) and is unique to BACON that produces multi-scale intermediate outputs, unlike the existing architectures such as SIREN that needs to go through the entire network for all cases. We set τ to be 0.7 times the finest voxel length.

2.4.2 Multi-scale SDF Evaluation

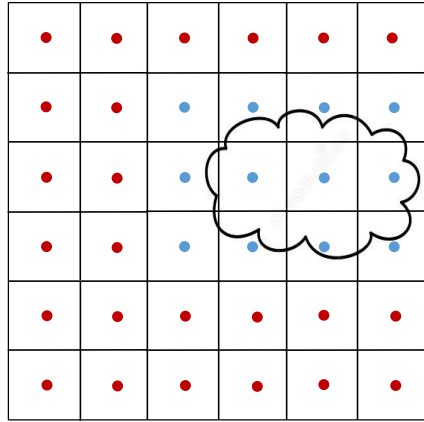
We introduce another strategy to accelerate Marching Cubes mesh extraction using octree-style, multi-scale SDF grids. As shown in Fig. 13, we evaluate the shape SDFs in a hierarchical way, from the low to high resolution grids. We note that the SDFs evaluated at a coarse level can be used to decide whether or not to subdivide a cell. That is, assuming the modeled SDFs are accurate, when the magnitude of SDF at the center of a voxel is larger than the radius of the circumsphere, the voxel is empty (i.e., containing no zero-level-set), so we do not need to further evaluate the SDFs at higher resolutions. Similarly, when the SDF magnitude at the center is smaller than the threshold R , the voxel contains zero-crossing, so it needs to be evaluated at higher resolution via subdivision. Empirically, we set R to be 2 times the circumsphere radius, to provide a margin of safety to the SDF modeling errors. This multi-scale Marching Cubes approach is not unique to BACON and can be applied to other SDF-modeling networks such as SIREN. As shown in Table 6, the strategy reduces the computation time by a factor of ≈ 40 .

2.4.3 Combining the Two Strategies

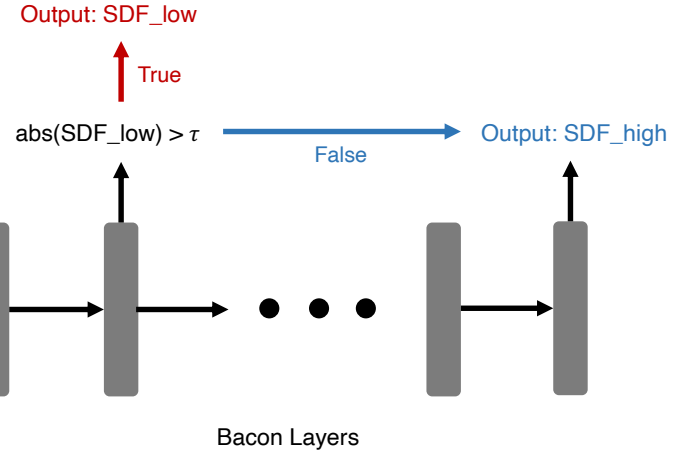
While the above two strategies individually provide significant speedup for mesh extraction, we can combine them together to further enhance the performance. That is, we adopt the adaptive-frequency approach for each level in the multi-scale evaluation. For coarse levels, we adopt the early-stopping strategy to all cells. For the finest resolution level, which takes account for most of the computations, we similarly adopt early-stopping for voxels that are far away from the zero-crossings using the threshold τ . As a result, the combination of the two strategies provide another meaningful reduction of computation time against the pure multi-scale scheme, as shown in Table 6. Note our accelerated Marching Cubes does not decrease the quality of the extracted meshes (see, output shapes in Fig. 14).

2.4.4 Discussion of Occupancy Networks

We notice that Occupancy Networks similarly proposed a multi-resolution mesh extraction strategy on the occupancy fields. The octree-style evaluation for occupancy fields could lead to errors, however, because occupancy fields do not provide the same empty-space guarantees that SDFs provide. Furthermore, the adaptive-frequency evaluation cannot be used for Occupancy Networks, and thus all query points need to be evaluated by the full network layers.



(a) Adaptive-Frequency Outputs



(b) Adaptive-Frequency Decision Process

Figure 12. Adaptive-frequency SDF evaluations. When evaluating SDFs on a dense grid (a) for mesh extraction, we leverage the band-limited nature of BACON layers to adaptively allocate the computation resources (b) across the cells. For each cell we first compute the SDF with a low-frequency output layer (SDF_{low}). For cells with the magnitude of SDF_{low} larger than some threshold τ (i.e., the red cells that are far from the zero-level-set), we do not proceed to the higher layers of BACON, as we do not need high-frequency details in the empty-space. For cells near the surface (i.e., when $|SDF_{low}| < \tau$), we compute the full-frequency SDF (SDF_{high}) using the highest layer output (the blue cells). This adaptive-frequency SDF evaluation saves significant amount of time on computing the SDFs in empty-space via early-stopping, which cannot be adopted by existing network architectures, e.g., SIREN, that need to go through the entire network layers for all evaluations.

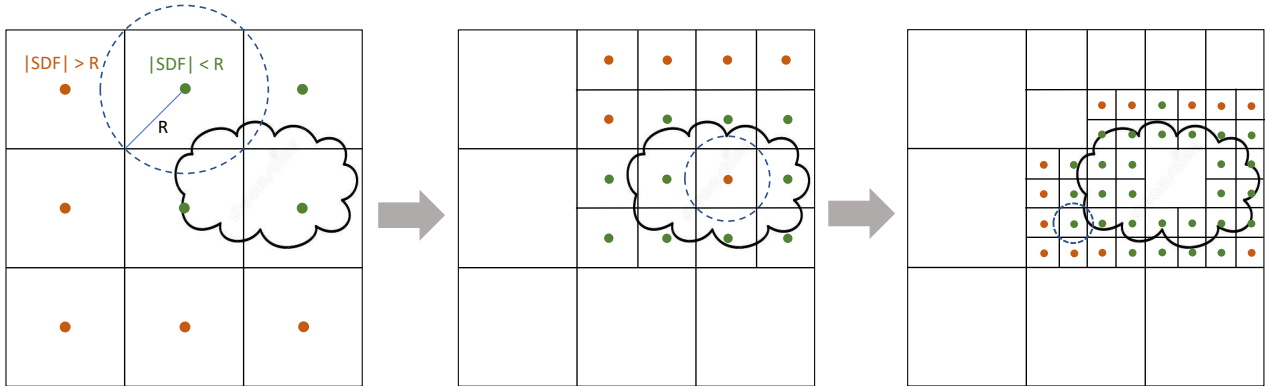


Figure 13. Multi-Scale Marching Cubes. We propose a hierarchical octree-style SDF evaluation scheme for efficiently pruning empty spaces using the nature of SDFs. We start from the coarsest resolution grid (left) and query the SDFs for all cells. Assuming the modeled SDFs are correct, we can identify some of the cells to be empty (i.e., no zero-crossing exists within the cell), when the magnitude of SDFs at the center is larger than the the radius of the circumsphere (dotted circles in the diagram). In practice, to provide a margin of safety for the model errors, we use $2 \times R$ for the criteria for checking empty cells. Then, only for the non-empty cells (green), we subdivide them into 8 cells and evaluate higher resolution SDFs in the next level grid, which we repeat multiple times. For all our experiments we used 4 levels of scales. Note that the proposed multi-scale SDF evaluation is not unique to BACON and can be applied to existing networks, e.g., SIREN, that model SDFs.

	Seconds				
	Armadillo	Dragon	Lucy	Sphere	Thai
SIREN Original	16.75	16.78	16.76	16.78	16.76
SIREN Multi-Scale	0.404	0.258	0.253	0.252	0.354
BACON Original	17.93	17.836	17.909	17.926	17.938
BACON Adaptive	5.925	5.325	5.278	5.391	5.584
BACON Multi-Scale	0.411	0.273	0.270	0.265	0.364
BACON Adapt. + Multi. (Proposed)	0.280	0.207	0.188	0.172	0.267

Table 6. Marching Cubes timing analysis. From top to bottom: dense vanilla Marching Cubes using SIREN; multi-scale Marching Cubes using SIREN; dense vanilla Marching Cubes using BACON; adaptive mesh extraction using BACON; multi-scale Marching Cubes using BACON; the proposed combination of multi-scale and adaptive SDF evaluation using BACON.

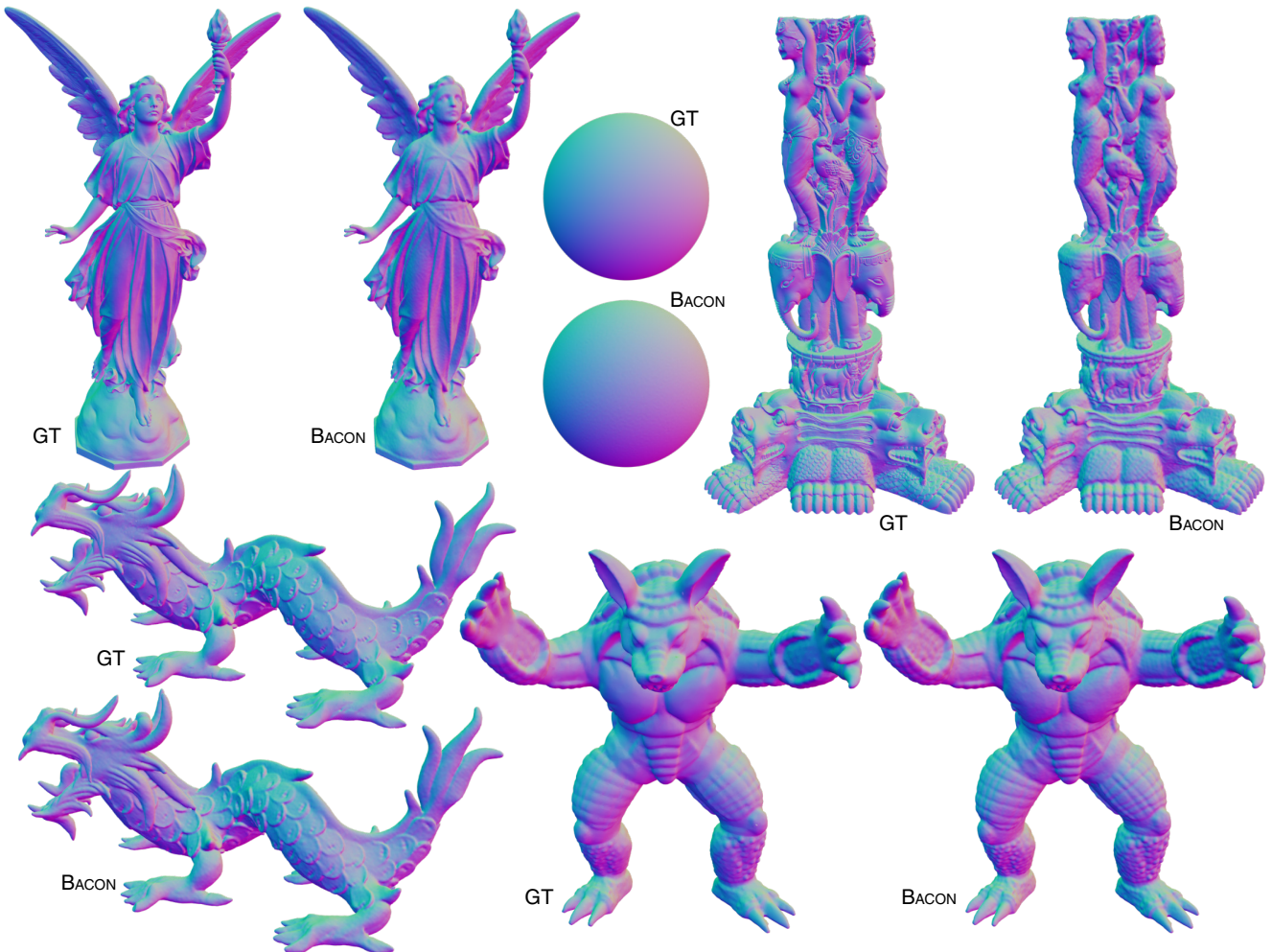


Figure 14. Extracted 3D shapes using the proposed adaptive-frequency multiscale inference procedure.

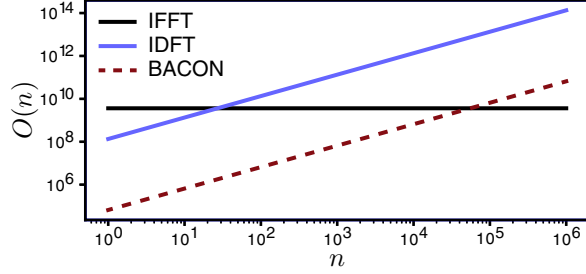


Figure 15. Comparison of asymptotic computational complexity.

2.5. Comparison to Explicit Fourier Basis

Interestingly, we find that a BACON representing a grid of 512^3 discrete frequencies (used in our shape fitting experiments) is more efficient to evaluate for few samples than using the Inverse Fast Fourier Transform (IFFT) or naive computation of the inverse discrete Fourier transform (IDFT) on an explicit grid of 512^3 coefficients. The computational complexity of the IFFT and IDFT are $O(N \log(N))$ and $O(N^2)$, where here, $N = 512^3$. BACON is a compressive representation of the spectrum, and its complexity scales as $O(d_h^2)$ (due to matrix multiplication). In Fig. 15 we plot a comparison of asymptotic computational complexity for n output samples for each of these methods. Since the IFFT always computes 512^3 outputs, its cost is constant.

References

- [1] Eirikur Agustsson and Radu Timofte. Ntire 2017 challenge on single image super-resolution: Dataset and study. In *CVPR Workshops*, 2017. 10
- [2] Robert B Ash, B Robert, Catherine A Doleans-Dade, and A Catherine. *Probability and measure theory*. Academic Press, 2000. 4
- [3] Jonathan T. Barron, Ben Mildenhall, Matthew Tancik, Peter Hedman, Ricardo Martin-Brualla, and Pratul P. Srinivasan. Mip-NeRF: A multiscale representation for anti-aliasing neural radiance fields. In *Proc. ICCV*, 2021. 10, 11, 13, 15
- [4] C. Chatfield and C. M. Theobald. Mixtures and random sums. *Journal of the Royal Statistical Society: Series D (The Statistician)*, 22(4):281–287, 1973. 4
- [5] Rizal Fathony, Anit Kumar Sahu, Devin Willmott, and J Zico Kolter. Multiplicative filter networks. In *Proc. ICLR*, 2020. 8, 9
- [6] Leo A Goodman. On the exact variance of products. *Journal of the American statistical association*, 55(292):708–713, 1960. 7
- [7] Geoffrey Grimmett and David Stirzaker. *Probability and random processes*. Oxford university press, 2020. 6
- [8] Peter Hedman, Pratul P. Srinivasan, Ben Mildenhall, Jonathan T. Barron, and Paul Debevec. Baking neural radiance fields for real-time view synthesis. In *ICCV*, 2021. 13
- [9] Ben Mildenhall, Pratul P. Srinivasan, Matthew Tancik, Jonathan T. Barron, Ravi Ramamoorthi, and Ren Ng. NeRF: Representing scenes as neural radiance fields for view synthesis. In *Proc. ECCV*, 2020. 13, 15
- [10] Vincent Sitzmann, Julien N. P. Martel, Alexander W. Bergman, David B. Lindell, and Gordon Wetzstein. Implicit neural representations with periodic activation functions. In *Proc. NeurIPS*, 2020. 9, 10, 11, 17
- [11] Towaki Takikawa, Joey Litalien, Kangxue Yin, Karsten Kreis, Charles Loop, Derek Nowrouzezahrai, Alec Jacobson, Morgan McGuire, and Sanja Fidler. Neural geometric level of detail: Real-time rendering with implicit 3D shapes. In *Proc. CVPR*, 2021. 17, 18
- [12] Matthew Tancik, Pratul P. Srinivasan, Ben Mildenhall, Sara Fridovich-Keil, Nithin Raghavan, Utkarsh Singhal, Ravi Ramamoorthi, Jonathan T. Barron, and Ren Ng. Fourier features let networks learn high frequency functions in low dimensional domains. In *Proc. NeurIPS*, 2020. 10, 11, 17